Impacts of aerosol particles on the microphysical and radiative properties of stratocumulus clouds over the southeast Pacific ocean

C. H. Twohy[1], J. R. Anderson[2], D. W. Toohey[3], M. Andrejczuk[4], A. Adams[1], M. Lytle[1], R. C. George[5], R. Wood[5], P. Saide[6], S. Spak[6], P. Zuidema[7], and D. Leon[8]

1) College of Earth, Oceanic and Atmospheric Sciences, Oregon State University, Corvallis, Oregon, USA. Correspondence: twohy@coas.oregonstate.edu
2) School for Engineering of Matter, Transport and Energy, Arizona State University, Tempe, Arizona, USA
3) Department of Atmospheric and Oceanic Sciences, University of Colorado, Boulder, Colorado, USA
4) School of Earth and Environment, University of Leeds, Leeds, UK. (Currently at Atmospheric, Oceanic and Planetary Physics, Department of Physics, University of Oxford, Oxford, UK)
5) Department of Atmospheric Sciences, University of Washington, Seattle, Washington, USA
6) Center for Global and Regional Environmental Research, University of Iowa, Iowa City, Iowa, USA
7) Rosenstiel School of Marine and Atmospheric Sciences, University of Miami, USA
8) Department of Atmospheric Science, University of Wyoming, Laramie, Wyoming, USA

Abstract. The southeast Pacific Ocean is covered by the world's largest stratocumulus cloud layer, which has a strong impact on ocean temperatures and climate in the region. The effect of anthropogenic sources of aerosol particles such as power plants, urban pollution and smelters on the stratocumulus deck was investigated during the VOCALS field experiment. Aerosol measurements below and above cloud were made with a ultra-high sensitivity aerosol spectrometer and analytical electron microscopy. In addition to more standard in-cloud measurements, droplets were collected and evaporated using a counterflow virtual impactor, and the non-volatile residual particles were analyzed.

Many flights focused on the gradient in cloud properties on an E-W track along 20°S from near the Chilean coast to remote areas offshore. Mean statistics from seven flights and many individual legs were compiled. Consistent with a continental source of cloud condensation nuclei, below-cloud accumulation-mode aerosol and droplet number concentration generally decreased from near shore to offshore. Single particle analysis was used to reveal types and sources of the enhanced particle number. While a variety of particle types were found throughout the region, the dominant particles near shore were partially neutralized sulfates. Modeling and chemical analysis indicated that the predominant source of these particles in the marine boundary layer along 20°S was anthropogenic pollution from central Chilean sources, with copper smelters a relatively small contribution.

Cloud droplets were more numerous and smaller near shore, and there was less drizzle. Higher droplet number concentration and physically thinner clouds both contribute to the smaller droplets near shore. Satellite measurements were used to show that cloud albedo was highest 500-1000 km offshore, and actually lower closer to shore due to the generally thinner clouds and lower liquid water paths there.

Differences in the size distribution of droplet residual particles and ambient aerosol particles were observed, with particles extracted from droplets being slightly larger than below-cloud particles in the mean. By progressively excluding small droplets from the CVI sample, we were able to show that the larger drops, which initiate drizzle, contain the largest aerosol particles. Geometric mean diameters of droplet residual particles were larger than those of the below-cloud and above cloud distributions. However, a wide range of particle sizes can act as droplet nuclei in these stratocumulus clouds. A detailed LES microphysical model was used to show that this can occur without invoking differences in chemical composition of cloud-nucleating particles.

1 Introduction

Stratocumulus clouds play an important role in the Earth's radiation budget. Their ability to reflect incoming shortwave radiation from the sun helps to cool the surface of the planet and offset warming by greenhouse gases (Hartmann et al., 1992). The albedo of stratocumulus clouds is dependent on the liquid water path (LWP, vertically integrated liquid water content) and the effective droplet radius r_e (Stephens, 1978). Since aerosol particles act as cloud condensation nuclei (CCN), they influence both droplet number concentration and size. The first indirect effect of aerosols on clouds, recognized by (Twomey, 1974), postulates that an increase in cloud condensation nuclei for clouds with constant liquid water path will result in a decrease in r_e, and thus an increased albedo. While simple in theory, observations of this effect are confounded by variability in LWP over the short time and space scales accessible by aircraft measurements (Twohy et al., 2005;Stevens and Feingold, 2009). Satellite measurements, while able to measure over longer time and space scales, may suffer biases especially near broken clouds (Marshak et al., 2008;Twohy et al., 2009), which can artificially increase derived aerosol number concentration near clouds. Additionally, aerosol particles themselves may impact cloud LWP through radiative/microphysical interactions (Ackerman et al., 2000;Ackerman et al., 2003;Lee et al., 2009), and the sign of the LWP response can be positive or negative (Ackerman et al., 2004;Wood, 2007). Knowledge of the effects of atmospheric aerosols, particularly anthropogenic aerosols, on stratocumulus albedo is a prominent need for accurate climate change assessments (Solomon et al., 2007).

The southeast Pacific Ocean (SEP) is an ideal environment to study stratocumulus clouds because it has one of the world's most persistent and unexplored cloud decks (Huneeus et al., 2006;Wood et al., 2011b). Chile, which borders a large portion of the SEP, has an economy heavily based in mining copper and other metals (Schüller et al., 2008). These sources and various other industrial and urban activity produce primary and secondary aerosol particles including sulfate, organic, and industrial types (Schüller et al., 2008;Hawkins et al., 2010;Tsapakis et al., 2002). Under the predominately southeasterly flow regime, these particles have the potential to influence the SEP stratocumulus deck through their potential action as CCN. Satellite datasets predict high concentrations of cloud droplets in the near-coastal regions of the SEP that would be sufficient to perturb the diurnal mean reflected shortwave radiation by 10-20 W m^{-2} in the absence of liquid water changes (George and Wood, 2010). Additionally, aerosol pollutants may alter the formation and persistence of pockets of open cells (POCs) within stratocumulus (Stevens et al., 2005b;Wood et al., 2011a), potentially influencing cloud fraction and albedo.

Huneeus et al. (2006) found a spatial correlation between sulfur emissions and decreased effective radii off the Chilean coast measured by satellite remote sensors. Back-trajectory analysis suggested that near the Chilean shore, marine boundary layer air along the 20°S parallel is usually influenced by continental sources, and indeed, research aircraft measured higher aerosol concentrations and droplet concentrations near shore than farther offshore (Bretherton et al., 2010;Allen et al., 2011). Kleinman et al. (2011) noted that the near shore region was enhanced in carbon monoxide and sulfate particles, which they attributed to South American coastal pollution sources.

2 Methods and Objectives

A U.S. National Science Foundation C-130 aircraft operated by the National Center for Atmospheric Research collected data on the SEP stratocumulus deck during October and November of 2008. This was one component of the VAMOS Ocean-Cloud-Atmosphere-Land Systems (VOCALS) project, with the overarching purpose of improving understanding of SEP clouds and their simulation in global climate models (Wood et al., 2011b). One of the specific VOCALS goals was to determine how the continental pollution from industrial activity affected droplet size (and presumably albedo) in the stratocumulus layer offshore. In particular, the first portion of the following VOCALS hypothesis (1c) is examined here:

The small effective radii measured from space over the SEP are primarily controlled by anthropogenic, rather than natural, aerosol production, and that entrainment of polluted air from the lower free-troposphere is an important source of cloud condensation nuclei (CCN).

Other objectives of this work were to determine what sizes and types of particles act as cloud condensation nuclei near shore and how they affect not only droplet size and number, but drizzle rate and cloud albedo.

While a variety of aircraft participated in the VOCALS experiment, this paper focuses on the data collected from the C-130 aircraft to address this hypothesis. Data from C-130 flights that transited from near the Chilean coast to offshore along the 20^{o}S latitude line were used to examine gradients of cloud microphysical and aerosol properties relative to distance from the coast. Flights were based out of Arica, Chile (70^{o}W longitude), and extended as far as 85^{o}W, about 1600 km offshore. Level flight legs of ten minutes duration (about 70 km in horizontal extent) were made sequentially below, in, and above the stratocumulus cloud layer. Sub-cloud legs were at approximately 150 m altitude, while in-cloud legs were about 300 m above cloud base as measured by soundings through the layer. The above-cloud legs were about 300 m above cloud-top, in free tropospheric air. For the purpose of our analysis, each leg was considered a sampling period, and 1 Hz data from the various probes were averaged over the entire leg as long as in-cloud data were available. Data from about 50 sub-cloud and cloud legs were composited to statistically evaluate changes with distance from shore (with actual number of samples varying slightly depending on the parameter due to measurement availability).

A wing-mounted Particle Measuring Systems (PMS) Passive Cavity Aerosol Spectrometer Probe (PCASP-100), and a cabin mounted Ultra High Sensitivity Aerosol Spectrometer (UHSAS) counted and sized particles from 0.1-3.0 μm and 0.055-1.0 μm dry diameter, respectively. For smaller particles, a Thermo-Systems Inc. 3760A Condensation Particle Counter (CPC) was utilized to quantify total particle concentration larger than 0.01 μm in diameter. Cloud droplets between 2 and 50 μm in diameter were measured optically using a Droplet Measurement Technologies Cloud Droplet Probe

(CDP). Drizzle drops larger than about 60 μm were measured using a modified PMS 2D-C optical array probe. Cloud droplets between about 7 and 50 μm in diameter were collected and evaporated with a counterflow virtual impactor, CVI (Twohy et al., 1997). The lower size limit was sometimes increased by the operator to investigate changes in properties with droplet size. The CVI inlet was heated to about 55°C in order to evaporate liquid water present in droplets (which also are impacted into dry air inside the CVI). At 55°C, some volatile organic species may be evaporated, in addition to water. However, organic material comprised a relatively small fraction of submicron aerosol mass in the VOCALS sampling region (Allen et al., 2011). The size distribution of non-volatile residual particles was measured with the pre-calibrated UHSAS.

Both ambient and CVI residual particles were collected with a three-stage micro-impactor (California Measurements, Model MPS-3) and a single stage filter sampler (PIXE International, Streaker Air-Particulate Sampler) operated in discrete mode under computer control. For the micro-impactor samples, particles impacted on the second stage (~0.5 to 1.0 μm diameter) and third stage (smaller than ~0.5 μm) were analyzed by transmission electron microscope (TEM, JEOL Model 2010) and elemental X-ray analysis (by energy dispersive spectrometer, EDS) on a number of flights. Selected filter samples were analyzed by automated scanning electron microscope (SEM, JEOL Model JSM-5800) controlled by a spectral imaging system (ThermoElectron NORAN System 7) and with a large-window silicon drift detector for EDS. The general approach of the automated SEM techniques are described by Anderson et al. (1996).

Two types of numerical models were utilized in this work. First, simulations using the WRF-Chem v3.3 model (Grell et al., 2005;Skamarock et al., 2008) provided high-resolution meteorology for trajectory analysis and were used to perform sensitivity analysis on the impact of smelter emissions on particle concentrations in the VOCALS sampling region. The WRF-Chem model was configured with 12 km horizontal resolution and uses the CBMZ-MOSAIC (Zaveri et al., 2008;Zaveri and Peters, 1999) framework for gases and aerosols. Smelter emissions were released as SO_2, which is converted to sulfate through gaseous (Zaveri and Peters, 1999) and aqueous chemistry (Fahey and Pandis, 2001) and reacts to form new particles, as well as condenses on existing particles. The model considers both the direct (Fast et al., 2006) and indirect effects (Chapman et al., 2009) of aerosols. Details on this configuration and validation against VOCALS measurements are thoroughly described in Saide et al. (2012).

In addition, a Lagrangian cloud model (LCM) utilizing a large eddy simulation (LES) numerical model with Lagrangian representation of microphysics (Andrejczuk et al., 2008) (Andrejczuk et al., 2010) was used to simulate droplet activation and evolution in VOCALS stratocumulus. The microphysical scheme tracks millions of groups of particles and is coupled with Eulerian dynamics and thermodynamics (Reisner et al., 2005). Depending on environmental conditions supplied by the Eulerian part of the model, water can condense/evaporate from the surface of particles, and forces resulting from the phase change, together with the drag forces, are returned to the Eulerian part of the model. For each group of particles, a full condensation model is included, meaning aerosol chemical properties are taken into account when solving the droplet

198 growth equation; however no subsequent chemical reactions are included. The three-
199 dimensional, horizontally periodic model domain was 3.2 km x 3.2 km in horizontal
200 extent and 2 km vertically, resolved with 80 x 80 x 200 grid points.
201
202 George and Wood (2010) used MODIS satellite data to show that variability in cloud
203 fraction is an important factor in the planetary albedo (including cloudy and clear areas)
204 of this region. Because we focus on aerosol effects on cloud properties, clear-air
205 regions are not included in flight-leg averages presented here. Further analysis of
206 MODIS-derived cloud albedos are presented in this work using the approach described
207 in Section 3.4.
208
209 Throughout the paper, correlations between various aerosol and cloud properties and
210 distance from shore are presented. Statistical significance for each relationship is
211 assessed in Table 1 using a simple one-tailed t-test at a probability level of 0.05. If the t
212 value for the observations, *tobs*, is greater than the critical t value, *tcrit*, the correlation
213 may be considered significant. Equations for significant relationships are also included.
214
215
216 **3 Results**
217
218 3.1 Changes in aerosol and cloud characteristics with distance from coast
219
220 Flights along the 20°S latitude line typically showed a steady and reproducible decrease
221 in droplet number concentration, N_d, when the C-130 aircraft flew from near the coast to
222 a remote region offshore. A corresponding increase in N_d was observed on return flights
223 within the boundary layer back toward shore. The number concentration of
224 accumulation-mode aerosol particles below cloud was also higher near shore than
225 offshore. Fig. 1a shows the mean aerosol particle number concentration, N_p, measured
226 below cloud vs. distance from shore (or longitude) using data from eight C-130 flights.
227 Both the PCASP (larger than 0.1 μm) and UHSAS (larger than 0.055 μm) data are
228 shown. The concentration minimum between the smaller Aitken mode and larger
229 accumulation mode begins at approximately 0.08 μm (Kleinman et al., 2011) in this
230 region. Therefore, the PCASP measures most, but not all, of the accumulation mode,
231 while the UHSAS measures all the accumulation mode and the tail end of the Aitken
232 mode. Below-cloud drizzle events were excluded from the aerosol data compiled.
233
234 N_p (>0.055 μm) decreased from about 400 to 600 cm^{-3} near shore to 100 to 200 cm^{-3}
235 ~1500 km offshore. This suggests, but doesn't alone establish, that the continent is the
236 dominant source of accumulation-mode particles near shore. Allen et al. (2011) and
237 Kleinman et al. (2011) found that both carbon monoxide (a continental tracer) and
238 sulfate aerosol mass also were higher in the boundary layer near shore than offshore.
239 While sulfate aerosol can be produced from plankton-derived dimethylsulfide or DMS,
240 Yang et al. (2011a) showed that DMS actually tended to be lower nearshore than
241 offshore. These facts, together with the back-trajectories presented by Bretherton et al.
242 (2010), Allen et al. (2011), and below, substantiate the hypothesis that the enhanced
243 accumulation-mode particles near shore are derived from continental and not marine

sources. Model studies with interactive aerosols and cloud microphysics have also simulated enhanced aerosol loadings associated with coastal pollution outflow events (Saide et al., 2012).

Smaller particles, down to ~0.01 μm diameter as measured by the CPC, were sometimes present in higher concentrations offshore than nearshore (Fig 1b). This indicate other sources of these ultrafine particles, such as entrainment from above the boundary layer or photochemical production within clean regions, for example in pockets of open cells (Berner et al., 2011). While relationships between N_p larger than 0.1 and 0.055 μm and distance from shore are both significant, total particles larger than 0.01 μm show no significant trend.

Fig. 1c shows that cloud droplet number concentration also increased with proximity to shore, in accordance with the trend in larger particles. Cloud and particle concentrations were not only highly correlated with distance from shore but also with each other (Fig. 1d). For the PCASP measurements, we have included a logarithmic as well as a linear fit to compare with Hegg et al. (2012), who presented sub-cloud PCASP concentrations vs. droplet concentration from the Twin Otter aircraft. The Hegg et al. (2012) study yielded a higher slope (0.72 vs. 0.44), but they used maximum measured droplet concentrations. Here we prefer to use mean droplet concentrations, as more representative of the variability of the entire cloud deck. In addition, the non-linear fit is more physical at low concentrations (e.g., with an intercept allowing particles to exist without droplets rather than droplets existing without particles). A polynomial fit is also included, as was used in Twohy et al. (2005) for stratocumulus off the coast of California. While the polynomial fit results in a slightly higher coefficient of determination (r^2) value than the logarithmic or linear fit, it would not be suitable to use at higher particle concentrations due to rollover. The range of below-cloud aerosol particle and droplet concentrations in the VOCALS region was similar to that measured in the northeast Pacific. However, at low aerosol concentrations, VOCALS clouds had higher droplet concentrations.

Table 1 shows that the relationship between measured $N_p > 0.1$ μm and droplet concentration is statistically significant. A similar strong relationship also applies between measured $N_p > 0.055$ μm and droplet concentration. Single particle analysis (Section 3.2) showed that the number concentration of accumulation-mode particles near shore was dominated by particles composed primarily of sulfate. These large, soluble particles are efficient cloud condensation nuclei and explain the strong correlation between accumulation-mode aerosol concentration and droplet number concentration along 20ºS, which has also been observed in other stratocumulus regions (Twohy et al., 2005;Hegg et al., 2012).

Note that the CDP may underestimate droplet concentration and overestimate droplet size due to the occurrence of coincident particles in the instrument sample volume (Lance et al., 2010). However, this effect is expected to be relatively small for the droplet concentrations <250 cm^{-3} that were measured by the C-130.

Both droplet mean diameter and the radiatively important droplet effective radius (r_e) increased with distance from shore (Fig. 2a) and decreased with N_p larger than 0.055 or 0.1 μm in diameter. This is in accordance with the expected Twomey effect, with increasing cloud condensation nuclei producing smaller droplets. However, as discussed in Sect. 3.4, other factors also play a role. As observed by others (Bretherton et al., 2010), drizzle drops were generally larger and often more prevalent offshore (Fig 2b). A tendency offshore toward stronger longwave cooling, entrainment and turbulence (Bretherton et al., 2010) provides more condensate to the layer, and some droplets grow large enough to initiate collision/coalescence and eventually grow to drizzle sizes. This process is inhibited near shore in the more polluted, smaller droplet clouds. However, cloud macroscale properties (Section 3.4) and mesoscale features (Comstock et al., 2007) can also impact droplet size, and drizzle is quite variable in the offshore region. Relationships between distance from shore and droplet mean diameter, effective radius, and drizzle size were also significant. Drizzle concentration, however, was much more variable and was only weakly correlated with distance from shore, at least for this data set.

3.2 Aerosol types and chemistry

3.2.1. Electron microscopy

Single-particle techniques are useful in investigating individual particles likely to act as cloud condensation nuclei, since mass measurements may be dominated by only a few larger particles. Highlights of the extensive TEM and SEM analyses of particles collected in the VOCALS region are given below.

During more pristine conditions, for example, those encountered well offshore on flight 11 (9 Nov 2008), TEM revealed that submicron clear-air particles and CVI cloud droplet residuals were dominated by sea-salt, with ammonium sulfate and bisulfate also present at sizes smaller than about ~0.2 μm. Sea-salt particles as small as 0.05 μm were also present. In apparently more polluted air masses, ammonium sulfate, potassium sulfate, black carbon and non-volatile organic particles smaller than 0.5 μm were observed in both CVI and ambient samples (Fig. 3). Potassium sulfate and organic particles containing potassium and sulfate are generally good markers for biomass burning, e.g., Silva et al. (1999). Sulfate was often internally mixed with sea-salt, in excess of sea-water ratios. This internal mixing could occur either through aqueous-phase oxidation of sulfur dioxide under VOCALS conditions (Benedict et al., 2012) or through coalescence scavenging of large droplets, more likely to form on sea-salt, with smaller droplets more likely to form on sulfate, e.g, Twohy et al. (1989a). Sea-salt was sometimes internally mixed with black carbon, most likely from urban pollution or shipping emissions.

Samples were taken above the stratocumulus layer as well. Trajectories reaching above cloud along 20ºS originated from more diverse locations (northerly, southerly or westerly) than those reaching in the boundary layer, which originated primarily from the south (Bretherton et al., 2010). Above-cloud particles were comprised of soil dust, acidic

sulfates, biomass burning and organics, reflecting their diverse origins. Industrial particle types containing aluminum, tin, iron and zinc were sometimes present both in particles above cloud, as well as in the marine boundary layer.

The TEM provides detection of smaller particles and better images than scanning electron microscopy (SEM), but the latter technique has been automated so that large numbers of particles can be analyzed via X-ray analysis. Therefore, more quantitative statistics can be obtained with SEM. Fig. 4 shows the percentage of particles by number in two different SEM size ranges for below-cloud samples collected near shore on C-130 flights 3 and 4 (21 Oct and 23 Oct 2008). For these samples, the SEM was configured for higher sensitivity to measure particles down to ~0.1 μm in size. Small particles were usually comprised of sulfate, and larger ones of sulfate and/or sea-salt. On the more heavily polluted 23 Oct flight, sulfate dominated over sea-salt (by number) in the larger particle size range as well. Sulfate and sea-salt are also expected to be internally mixed with some volatile organic material not detectable by this technique; however, submicron organic aerosol mass was typically only about 10% of total submicron aerosol mass within the VOCALS region (Allen et al., 2011;Yang et al., 2011b).

3.2.2 Measurements and modeling related to smelter emissions

Along the 20ºS parallel, air in the marine boundary layer (MBL) east of ~76ºW has typically traveled from central Chile (south of 28ºS), while air father west usually originates over the open ocean (Bretherton et al., 2010;Allen et al., 2011). Two to five days after emission, continental SO_2 emissions are expected to be nearly completely converted to sulfate (Saide et al., 2012). These sulfate plumes and their influence on clouds can be seen in NOAA ship observations and cloud satellite retrievals, as presented in a comparison between models and measurements by Saide et al. (2012).

The VOCALS experimental design document hypothesized that *"strong sulfur emissions from Chilean and Peruvian copper smelters lead to strongly polluted conditions near the coasts."* Emissions from smelters include primary aerosol particle emissions, as well as gaseous SO_2 that can be rapidly converted to sulfate aerosol. Anderson et al. (1988) showed that approximately 80 km downwind of copper smelters in the western United States, particles between about 0.4 and 1.0 μm in diameter were enhanced in lead (detectable in about 10% by number of particles measured) and copper (about 6% by number). Levels of particulate lead from the only smelter covered by the Anderson study still operating today continue to be high (unpub. data, Arizona Dept. of Environmental Quality), despite significant improvements in emission controls.

Automated SEM results from over 70,000 particles on eight different C-130 flights from a variety of levels and locations in the VOCALS study region were examined for the presence of copper and lead. The detection limit for copper with the large-window silicon drift EDS employed is about 0.2 to 0.4 weight percent (wt%) relative to a known standard of effectively infinite thickness. 0.4 wt% copper was used to filter the 70,000+ particles. Lead had a slightly higher detection limit than copper (0.5 wt%). The apparent

total wt% of a particle depends its size, composition and, to some extent, its morphology. Based on simple regression analysis and excluding oxygen and carbon, the total wt% of an average 0.5 μm diameter non-carbonaceous particle is 4.2. A typical 1.0 μm diameter particle has an apparent total wt% of 8.0.

Of the 70,000 particles analyzed, only 0.1% contained detectable Pb and only about 0.1% contained detectable Cu. Particulate lead can come from a variety of sources, and urban pollution aerosols can contain Cu-bearing particles from vehicular sources (such as brake pad wear) and non-vehicular sources, e.g., Anderson et al. (2006). In contrast, about 2% of analyzed particles contained Si, a marker for soil dust from continental sources. For these VOCALS SEM samples, particles were analyzed down to ~0.2 μm in diameter, a smaller size than analyzed in the (Anderson et al., 1988) study. However, these results suggest that copper smelters may not have been such a large influence in the VOCALS region as was originally thought.

The VOCA emission inventory identifies pollutant contributions by source sector and location (http://www.cgrer.uiowa.edu/VOCA_emis/). Several large copper smelters in northern Chile and Peru account for the majority of regional SO_2 emissions. FLEXPART forward trajectories (Stohl et al., 2005) (Fast and Easter, 2006) were driven by the Weather Research and Forecasting model meteorology (Saide et al., 2012) for major smelters in the region. The largest, Ilo, is located to the north of the study region with trajectories to the northwest, while the others (Chuquicamata and Potrerillos) are at elevations that lead to eastward advection over the South American continent (Fig. 5). Trajectories from these sources may have a southward meridional component (Toniazzo et al., 2011) that could take pollution from these sources to latitudes where they can be transported to the study area, but the eastward component dominates. In episodic cases where the southward flux dominates, the plume would be diluted and mixed with fresh emissions that, as discussed below, are also further diluted by the time the plume reaches the VOCALS study area. Even when plumes from northern sources do reach the Pacific, they advect northward with the mean meridional flow (Spak et al., 2010). Thus, we may conclude these northern smelters rarely impacted VOCALS flights along 20°S. There are, however, three copper smelters in central Chile, Caletones, Ventanas, and Chagres, with SO_2 emissions of 108, 10.6, and 3.2 Gg/yr, respectively. These represent about 47% of SO_2 emissions from central Chile. The largest smelter in the region, Caletones, is located in the Andes foothills south of Santiago at 1700 m ASL. The FLEXPART trajectories show that air originating at Caletones either crosses eastward into Argentina or may occasionally be entrained into the southeast Pacific MBL east of 75ºW (approximately half of the study days), depending on the location of the subtropical Pacific high (Spak et al., 2010).

To explore further, FLEXPART back dispersion analysis was carried out with 10,000 trajectories (not shown) originating from times and locations where electron microscopy samples were taken from the C-130 aircraft. Results indicate that when the measurements are affected by inland sources, other coastal sources have a higher impact than smelters in the Andes such as Caletones. These include area sources, coastal power plants, steel mills and industrial boilers. Smelter emissions present over

the study region would have been highly diluted, aged, and mixed with primary and secondary aerosols from other sources that have similar emissions rates but are less diluted and aged upon arrival.

Results from WRF-Chem model also suggest that smelters were not the major source of enhanced particles over the ocean along 20°S. Fig. 6 shows the mean % difference for particle number concentration in the boundary layer predicted with and without smelter emissions included for WRF-Chem model runs of 15 Oct 2008 to 15 Nov 2008, the time period coinciding with the VOCALS C-130 flight dates. The size range considered is the same as for the PCASP instrument, 0.12 to 3.0 μm diameter. Along 20°S, smelters are predicted to enhance number concentration over the ocean by only 15 to 20% at most (between about 71°W and 77°W). Interestingly, a slightly larger effect is seen both to the north and to the south of the 20°S line where the intensive VOCALS measurements focused. The largest effect of smelter emissions is predicted to be near shore around 17°S, downwind of the Ilo smelter, and over land near Chuquicamata, where trajectories tend to recirculate.

Fig. 7 shows the mean predicted values in 2.5° increments with and without smelter emissions in the boundary layer along the 20°S parallel. Particle number concentration (0.12 to 3.0 μm) is given in Fig. 7a and sulfate mass in Fig. 7b. The absolute change in particle number concentration due to smelter emissions is at a maximum at 72.5°W (near the shoreline), where smelters are predicted to typically contribute about 68 cm^{-3} to the available particle population of about 320 cm^{-3} total (21%). Sulfate mass at 72.5°W, on the other hand, is predicted to increase by 40% with smelter emissions included, indicating that a substantial fraction of sulfur may deposit on existing particles downwind of the smelters themselves. The mean change along 20°S between 70°W and 85°W where the C-130 aircraft measurements were made was 13% for particle number and 28% for sulfate mass. The impact of smelter emissions (not shown) is predicted to be somewhat larger in the free troposphere than in the marine boundary layer, with number concentration being impacted the most by 42% at 72.5°W and by 34%, on average, between 70°W and 85°W.

The WRF-CHEM-predicted particle concentrations from smelters, while not very large, are greater than the very small fraction of particles containing copper or lead detected via SEM. There are several probable reasons for this result. The larger, primary particles that serve as distinct tracers for smelting are likely diminished after several days of dilution, cloud processing and wet deposition. On the other hand, the secondary particles produced from SO_2 by oxidation and condensation are smaller and may be produced farther downwind, in addition to near the source. Thus, they would be not necessarily have been detected in the Anderson et al. (1988) study, which measured particles larger than 0.4 μm, relatively close to the smelter itself. Possible uncertainties in model treatment include an overestimation of source emissions (Saide et al., in press) and a shallower than observed near-shore marine boundary layer (Saide et al., 2012); both of which could cause higher particle number concentrations. Given these factors, the percentages contributed by smelters given in Figs. 6 and 7 can be considered to be upper limits. The electron microscopy and WRF-Chem results together

474 indicate that different emissions, such as those coming from other central Chilean
475 sources, were the major cause of the enhanced accumulation-mode particle
476 concentrations observed nearshore along 20°S.
477
478
479 3.3 Aerosol size distributions
480
481 3.3.1 Dependence of residual particle size on droplet size
482
483 The particle critical supersaturation, S_c, is the supersaturation with respect to water that
484 is necessary for a particle to grow from a stable deliquesced particle into a larger cloud
485 droplet. Given the same chemical composition, Köhler theory predicts that the largest
486 particles, which have a lower critical supersaturation, will be more active in forming
487 droplets (Wallace and Hobbs, 1977). In addition, the larger particles are expected to
488 form larger droplets in the initial stages of cloud formation (Twohy et al., 1989a).
489 Subsequent in-cloud processes, such as mixing of air parcels with different histories
490 and chemical reactions may modify, but not completely eradicate, this size dependence
491 (Ogren and Charlson, 1992). To explore these processes in more detail, we chose
492 periods of relatively stable cloud properties (droplet number concentration and liquid
493 water content) to investigate the distribution of activated droplets in stratocumuli during
494 VOCALS flights. Increasing the counterflow rate out tip of the CVU inlet progressively
495 increases the “cut size”, rejecting smaller droplets, while retaining larger droplets. The
496 cut size is defined as the size of droplet that is collected with 50% efficiency by the CVI,
497 and is based on laboratory and theoretical calculations (Noone et al., 1988;Anderson et
498 al., 1993).
499
500 Fig. 8 shows the droplet residual size distribution as a function of changing droplet cut
501 size for two VOCALS flights in the near-shore region. At the minimum droplet cut size of
502 about 7 μm diameter, a broad range of particle sizes are present within droplets, down
503 to the 0.055 μm lower limit of the optical particle counter. As smaller droplets are
504 excluded, smaller residual particles are also excluded, and the mean particle size
505 increases. At the largest droplet sizes, only the large particles are primarily present, with
506 mean sizes of 0.276 μm and 0.316 μm for the two cases shown. These larger particles
507 within larger droplets are consistent with simple droplet activation and growth theory,
508 e.g., Twohy et al. (1989a). While these large droplets are relatively few in number, they
509 are important, as they are the ones that will initiate drizzle. Additionally, they are
510 expected to be different chemically due to differences in particle composition with size.
511 For example, Twohy et al. (1989a) showed that larger droplets should preferentially
512 form on sea-salt, rather than typically smaller sulfate. These alkaline droplets would
513 initially contain a large fraction of available S(IV) (aqueous SO_2, bisulfite and sulfite) in
514 the cloud, which may be converted irreversibly to sulfate through aqueous-phase
515 reactions (Hegg and Hobbs, 1979). As shown in Fig. 4, VOCALS samples near shore
516 showed evidence of this occurring, with chloride in many particles being at least partially
517 replaced by sulfate. Through this process, sea-salt acts as a sink for SO_2 and may limit
518 the formation and growth of smaller sulfate aerosols (Yang et al., 2012).
519

3.3.2 Below cloud vs droplet residual size distributions

It is also of interest to compare the dry size distributions of below-cloud aerosol particles with those produced from evaporated droplets within the cloud. In-cloud periods where electron microscopy samples were obtained were matched to the closest available below-cloud period where UHSAS data were available. Samples used in this analysis were primarily, but were not limited to, those taken during flights along the 20°S parallel. In-cloud samples were 3-7 minutes in duration (about 20 to 47 km) while below-cloud samples were 2-4 minutes in duration (about 14 to 27 km). The mean time between in-cloud and below cloud samples was 18.5 min (about 125 km).

Drizzle drops can break up within inlets and produce particulate artifacts downstream (Clarke et al., 1997;Weber et al., 1998;Hudson and Frisbie, 1991). For the CVI inlet, modeling (Kulkarni and Twohy, 2011) and measurements (Twohy et al., 2003) indicate that drops larger than ~100 μm are prone to break up. Thus, time periods with significant drizzle were excluded from in-cloud samples, using two screening criteria that both needed to be met for samples to be accepted. First, mean drop number concentration from the 2D-C probe was required to be < 5 lit^{-1}. The 2D-C probe measures the 60 μm to 800 μm diameter drop range where the drizzle mode presides, and in VOCALS, low number concentrations were correlated with smaller drop sizes. As a second safeguard against any drizzle artifacts potentially remaining, the ratio of mean CVI total residual number to the droplet number concentration was required to be less than or equal to 1.0. The CVI number concentration was taken from the CPC downstream of the CVI inlet, while the droplet concentration was measured by the CDP (or FSSP if CDP was not operative). This screening resulted in 20 acceptable pairs of samples. The ratios of total CVI number, N_c, to CDP or FSSP droplet number, N_d, for these samples ranged from 0.38 to 0.96. Low ratios could occur because in polluted cases, droplets were sometimes smaller than the minimum cut size of the CVI, and higher cut sizes were sometimes intentionally used as discussed in the previous section.

Under a simplifying assumption of a lognormal distribution, the geometric mean diameter, d_g, was calculated for each UHSAS distribution. Aggregate statistics for all samples are compared in Fig. 9. As expected, residual particles from droplets tended to be larger than below-cloud particles. 50% of the below-cloud sample d_gs fell between 0.129 and 0.143 μm, with a median or 0.135 μm, while 50% of the in-cloud d_gs were between 0.136 and 0.160 μm, with a median of 0.148 μm. While none of the in-cloud d_gs were smaller than 0.127 μm, below-cloud d_gs were as small as 0.106 μm. Above cloud particles were even smaller than below-cloud particles, with a median d_g value of 0.102 μm for samples taken shortly before or after these cloud samples.

To investigate further, below-cloud and in-cloud size distributions are plotted for four sample sets with $0.72 \leq N_c/N_d < 0.94$ (i.e., when the CVI was collecting most droplets) in Fig 10. Plots a-d are ordered from the highest to lowest droplet concentration, representing mean N_d ranging from 292 cm^{-3} in Fig. 10a to 86 cm^{-3} for Fig. 10d. (Note

565 that some of the extremely clean clouds sampled in VOCALS—particularly in “pockets
566 of open cells”--could not be sampled reliably due to the ubiquitous drizzle present.)
567
568 Most of the non-drizzling cloud distributions show greater involvement of larger
569 particles in cloud formation, but there is considerable variability from sample to sample.
570 Additionally, the in-cloud distributions lack any clear cut-off diameter below which
571 particles are not activated. Particles down to the lower size limit of the UHSAS, 0.055
572 μm, appear to be involved in cloud formation, although in smaller percentages relative
573 to the available ambient aerosol than larger particles are. Even samples with extremely
574 low 2D-C concentrations, on order ~1 lit^{-1}, exhibit involvement of some small particles
575 in cloud formation. Also, the total residual numbers measured with the CPC indicate
576 that some droplet residuals are even smaller than 0.055 μm in size. This is important,
577 as it indicates at least some of the cloud nuclei are coming not from the accumulation
578 mode but from smaller particles, which may have different sources and compositions.
579 Analyses that assume only the larger, lower S_c particles influence CCN concentrations
580 (and thereby droplet number, size, drizzle concentration and radiative properties) may
581 be incorrect.
582
583 This ability of small particles to form droplets has been observed by others; for example
584 (Ostrom et al., 2000) found many particles smaller than 0.1 μm in diameter in
585 stratocumulus off the coast of California. This phenomenon may be due to a number of
586 factors. First, droplets with a range of histories are sampled within a single in-cloud
587 sample considered here, which comprises many horizontal km of cloud elements
588 containing both updrafts and downdrafts. Probability plots for measured 1 Hz in-cloud
589 vertical velocities during the four non-drizzling time periods are shown in Fig. 11. Each
590 sample is a mixture of cloudy air with a wide range of vertical velocity histories, each
591 with many updrafts and downdrafts. The probability plot format shows that for the four
592 samples, about 10 to 40% of the vertical velocities are >0.5 m s^{-1} and about 1-10% are
593 >1 m s^{-1}. At 1 m/s, supersaturations (S) of ~0.9% can be achieved in a low-aerosol
594 environment and S~0.4% in a high-aerosol environment (Chuang, 2006). These values
595 correspond to critical diameters as small as about 0.025 μm to 0.045 μm, respectively,
596 for sodium chloride particles and slightly larger sizes for ammonium sulfate (Hudson,
597 2007). The smaller size may be more likely to be activated in cleaner clouds offshore,
598 where higher supersaturations are reached for two reasons: there are fewer available
599 cloud condensation nuclei on which water can condense, and more variable and
600 sometimes stronger updrafts due to stronger dynamical forcing (Bretherton et al., 2010).
601 Higher updraft velocities are correlated with higher droplet concentrations in
602 stratocumulus (Leaitch et al., 1996;Snider and Brenguier, 2000), presumably due to the
603 activation of CCN with higher critical supersaturations, which are usually smaller in size.
604
605 A second factor is that in downdrafts and regions of entraining dryer air near cloud top,
606 particles of various sizes can be released from droplets through evaporation. This may
607 reduce the droplet number concentration; indeed, Leaitch et al. (1996) found that the
608 mean droplet concentration in marine stratus was only about half the maximum droplet
609 concentration for each in-cloud flight leg. The effect of mixing and subsequent
610 evaporation on the residual size distribution will vary depending on whether the mixing

611 is homogeneous, where small droplets evaporate completely, or inhomogeneous, which
612 seems to be common (Twohy and Hudson, 1995;Lu et al., 2011). In the extreme
613 inhomogeneous case, the parcel is essentially diluted, with a decrease in droplet
614 concentration, but no change in the percentage of large and small droplets. This could
615 result in a decrease in residual particles across all sizes, while retaining the small ones,
616 such as is seen to some extent in Figs. 10. The net effect on the residual size
617 distribution is similar to that expected from the mixing of particles with different histories
618 that occurs during sampling, as discussed above.
619
620 Entrainment of above-cloud air may not only evaporate existing droplets, but may be a
621 source of new CCN to the stratocumulus cloud layer (Clarke and Kapustin, 2002). Since
622 particles above cloud tended to be smaller than below cloud in the VOCALS region
623 (Allen et al., 2011), this process could also be a source of additional small particles in
624 the CVI residuals (see also modeling results, Sect 3.3.3).
625
626 Other factors that could influence the shape of the CVI residual size distribution include
627 differences in CCN chemistry, in-cloud chemical reactions (sulfate and organic aerosol
628 production), and coalescence. Larger sea-salt particles are expected to be better CCN
629 than smaller sea-salt particles; additionally, modeling shows small particles can be
630 present within droplets even without any variation in CCN properties. In-cloud chemical
631 reactions (Hegg and Hobbs, 1979) may be active in the VOCALS region (Benedict et
632 al., 2012), but would be expected to enhance the large residual particle population at
633 the expense of the small ones (Feingold and Kreidenweis, 2002). Thus, varying CCN
634 chemistry or in-cloud chemical reactions are unlikely to explain our results.
635 Coalescence, however, could create a relative enhancement of small residual particles
636 by removing larger particles from the cloud, a process explored further through
637 modeling, as described below.
638
639 3.3.3 Results of 3-D LCM/LES model with particle tracking
640
641 Initial conditions for the Lagrangian cloud model were derived from British BAE-146
642 measurements along the 20°S line during VOCALS on 13 Nov 2008 at 11:08:00-
643 11:28:00 and 11:47:00-12:02:00 UTC. These two periods showed contrasting droplet
644 concentrations in cloud and provided information about the aerosol distribution below
645 the cloud, as well as air temperature, humidity, velocity, and radiative fluxes. The
646 “HIGH” case at about 73°W had a mean cloud droplet concentration of 250 cm^{-3}, while
647 the “LOW” case at about 77°W had a droplet concentration of 65 cm^{-3}. The initial
648 aerosol distributions were assumed to be bimodal and composed of ammonium sulfate.
649 In addition to the below-cloud aerosol distribution, above cloud and the ocean surface
650 were also potential sources of particles. 3-D simulations were run for this paper, with
651 the horizontal velocity specified as (u,v) = (-1,1 m s^{-1}) for HIGH and (-3,4 m s^{-1}) for the
652 LOW. Longwave radiative forcing was based on the Stevens et al. (2005a)
653 representation, with parameters fitted to better reproduce observed radiative fluxes with
654 the following tuning parameters: F_0= 115 W m^{-2}, F_1=63 W m^{-2}, κ = 91 m^2 kg^{-1} for HIGH
655 and F_0=81 W m^{-2}, F_1=45 W m^{-2}, κ = 73 m^2 kg^{-1} for LOW. Eight hours of cloud evolution
656 were simulated, with spin-up in the model assumed to be complete after two hours. The

coalescence process is active from the beginning of the third hour, and in subsequent hours, the processes that may be important in real clouds can be examined. We note, however, that the large-scale subsidence and shortwave radiative forcing that can influence stratocumulus evolution are not included in these runs.

For comparison with the in-situ measurements shown in Fig. 10, the modeled size distributions of particles larger than 0.055 μm are shown in Fig. 12 for the two model cases, after two hours and eight hours of model simulation time. As in Fig. 10, the aerosol distribution below the cloud in shown with the blue line and aerosol particles within droplets (diameter > 8 μm) is the red line. The complete aerosol distribution (interstitial plus within droplets) in the cloud layer is shown as the green line. The below-cloud aerosol distributions used in the model, based on BAE-146 measurements, are slightly different from those observed on the C-130 for the periods shown in Fig. 10. Relative to the below-cloud distributions, however, the modeled in-cloud distributions are similar in shape to the observed distributions. In both cases, while larger particles tend to be more active in cloud formation, no sharp activation is observed at a single particle size. This wide range of within-droplet particle sizes occurs without invoking any difference in particle chemistry or hygroscopicity. Rather, it is likely due to the different thermodynamic histories of air parcels and the influence of coalescence, as described below. Results for the HIGH (panels a and b) and LOW (panels c and d) cloud droplet cases are similar. However, for the LOW case because of the fewer particles and higher in-cloud supersaturations, there is greater involvement of smaller particles in cloud droplet nucleation.

Some of the in-cloud CVI data (Fig. 10) look like the two-hour model simulations (after spin-up is complete), while others look more like the later simulations, with a broader, flatter appearance. The greater horizontal extent and therefore variable thermodynamic history for the CVI in-situ samples is one explanation for this; for example, the model never predicted vertical velocities larger than 1 m s^{-1}, while these were sometimes observed in the C-130 in-situ measurements (Fig. 11). Additionally, an active collision/coalescence and drizzle process occurring prior to sampling the actual clouds could produce this effect, as discussed below.

Over time, the difference between the initial below-cloud aerosol distribution and the aerosol distribution inside the droplets increases for both model cases. This difference is partially due to a change in the total particle distribution within the cloud as a result of aerosol processing by coalescence. The coalescence process moves many particles initially in the ~0.1 to 0.3 μm size range to a few larger particles, which eventually may be removed as drizzle. Fig. 13 shows the vertical profiles of total aerosol (activated and unactivated) predicted at 8 hours for the HIGH and LOW simulation. While initially the aerosol profiles are uniform throughout the boundary layer, over time, the aerosol particles just below and in the cloud layer are depleted relative to the near-surface layer. This is due to coalescence and drizzle removing particles from the cloud faster than they are replenished from the surface or from above the cloud.

We also investigated where the model predicted aerosol particles within cloud droplets to originate for the two simulations. The major source of the particle number

concentration within cloud droplets at all times was particles originating below the cloud. After 8 hours of simulation, about 20% of the aerosol within droplets could be attributed to other sources: for the HIGH simulation, this was primarily particles entrained from above the cloud, while for the LOW simulation, it was primarily particles generated from the ocean surface. Thus particle entrainment from above and particle generation from below may be small, but non-negligible sources of CCN.

3.4 Cloud thickness, liquid water path and potential radiative impact

Liquid water path, as well as cloud droplet effective radius, determine cloud optical thickness τ through the following approximation (George and Wood, 2010):

$$\tau \approx \frac{1.8\, LWP}{r_e \rho_w} \qquad (1)$$

Cloud optical thickness, in turn, determines visible cloud albedo or reflectance. The enhanced droplet number concentration and reduced droplet size observed in the VOCALS near-shore region would be expected to produce more reflective clouds if LWP stayed constant (or increased) relative to an unperturbed stratocumulus region. Typical levels of absorbing black carbon (<50 ng m^{-3}) measured from the C-130 in VOCALS (Shank et al., 2012) should have a negligible effect on cloud albedo (Twohy et al., 1989b).

LWP was derived for the 20°S missions from the G-band Vapor Radiometer (GVR) (Zuidema et al., 2012), supplemented by adiabatic LWP derived from the on-board radar (Wang et al., 2012) when GVR data were not available. The upward-looking radar and lidar (Wang et al., 2012) were used to estimate cloud thickness during the sub-cloud flight legs. While quite variable, generally both cloud thickness and the closely related LWP were smaller near shore for the VOCALS time period (Fig. 14a), with both being significantly correlated with distance from shore (Table 1). This change in cloud physical properties is observed in satellite data also (Painemal and Zuidema, 2010) and is probably related to the large scale meteorology; for example, the increased subsidence and thinner boundary layer near shore (Wyant et al., 2010;George and Wood, 2010). Some modeling studies have shown that higher aerosol concentrations may lead to smaller liquid water paths through enhanced entrainment of dry air (Ackerman et al., 2004) or reduced drizzle-driven turbulence and smaller moisture flux from the ocean surface (Jiang et al., 2002). However, during a series of VOCALS measurements at a fixed near-shore location (20°S, 72°W), (Zheng et al., 2011) found that LWP actually was positively correlated with aerosol concentration for a well-mixed boundary layer. The response of LWP to aerosol particles may even depend on the cloud base height (Wood, 2007).

Regardless of the still poorly understood cause, the generally thinner characteristic of the near-shore cloud field is very important in interpreting satellite measurements, which show small effective radii near shore. Due to condensational growth, droplet size

increases with depth throughout the cloud layer. As a result, clouds with smaller thicknesses and liquid water paths will, for a given droplet concentration, have smaller droplets. Returning to the VOCALS hypothesis presented earlier, it seems that the small effective radius near shore is not only due to the presence of anthropogenic pollutants increasing droplet number concentration, but also due to the large-scale forcing that causes clouds to be thinner near shore.

The relative contributions of increasing droplet concentration and decreasing cloud thickness in modifying the r_e of nearshore clouds can be estimated as follows. Since the VOCALS clouds tended to be quasi-adiabatic (Zuidema et al., 2012), changes in r_e can be related to changes in the height above cloud base, h, and droplet number concentration N_d through Eq. (11) of Brenguier et al. (2000):

$$r_e \propto \left(\frac{h}{N_d}\right)^{\frac{1}{3}} \quad (2)$$

Holding the nearshore cloud thickness constant at 200 m (Fig. 14a) while changing N_d from the unperturbed value of 80 cm^{-3} to the polluted value of 250 cm^{-3} (Fig. 1c) yields a decrease in r_e of 32%. Holding the nearshore N_d constant while changing the cloud thickness from 400 m to 200 m yields an r_e decrease of 21%. Thus about 60% of the net decrease in r_e can be attributed to the change in N_d (a microphysical change due to enhanced pollution), while about 40% is due to the smaller cloud thickness near shore, more likely a macroscale effect.

Top-of-cloud albedo, $A_{TOC,}$ was calculated for both the in-situ and MODIS satellite data as a function of τ (Eq. 1), using the delta-Eddington approximation following Eq. 37 of King and Harshvardhan (1986). Since r_e measured from the CDP during in-situ cloud legs is dependent on the sampling height and does not necessarily reflect the near-cloud-top value measured by satellite, r_e for the in-situ albedo calculations was derived from the aircraft-measured droplet number concentration and LWP, as described in George and Wood (2010). MODIS cloud albedo was also calculated, using LWP and r_e derived from the 10:30 AM local satellite overpass for one-degree increments along 20°S between 15 Oct to 15 Nov 2008. For comparison, the solar zenith angle at 10:30 local was used for both the satellite and in-situ albedo calculations.

Fig. 14b shows cloud albedos derived from the two techniques (in-situ and remote sensing). For the in-situ data, samples between 8:30 and 20:30 local time are plotted separately from 20:30 to 8:30 local time, since LWPs tend to be lower during daytime hours due to solar insolation (Wood et al., 2002). Albedo values were calculated during nighttime hours for completeness, as most of the data far offshore were collected at night. Results for satellite and in-situ data are similar in magnitude, particularly for near-shore clouds. The far-offshore albedos from the in-situ data are larger than those from MODIS at 10:30 local, a result of the large LWPs that tend to occur during nighttime hours. Additionally, the in-situ data points exhibit strong variability with a slight increasing trend offshore that is not statistically significant.

Using Fig. 14b and relying on the satellite data for a more statistically robust data set, relative to apparently unperturbed clouds 1000 km or farther offshore, MODIS cloud albedos (open squares) increase slightly between about 500 and 1000 km from shore. This corresponds to the region that Allen et al. (2011) named the "transitional" zone, between about 75ºW and 80ºW. Note in Fig 1b and 1c that droplet concentration is enhanced and droplet size is decreased in this region relative to the unperturbed clouds offshore. However, nearer shore, albedo decreases again substantially. Since droplet size is definitely smaller near shore (Fig 1c), this decrease in near-shore albedo must be due not to a droplet size effect, but to the decrease in cloud thickness and LWP which reduces the cloud optical thickness near shore (Eq. 1). The net effect of these factors is that cloud albedo actually tends to be smaller near shore, with a slight enhancement offshore where aerosol particles impact the droplet concentration, but clouds are still relatively thick.

The observation that an increase in albedo is not observed near shore relative to offshore does not mean, however, that present day pollutants are not changing cloud properties relative to pre-industrial values. If the pre-industrial droplet concentrations throughout the region were similar to those measured in unperturbed air offshore, a significantly smaller effective radius and lower cloud albedo would have existed at that time, if liquid water paths were similar to the present day (George and Wood, 2010). Thus, anthropogenic pollutants being produced today still may be producing a significant cloud brightening effect. The complex factors influencing cloud liquid water path (mesoscale variability, proximity to land, and even aerosol concentration), however, make this theory difficult to validate.

4 Summary and Conclusions

Particle number concentrations were observed to increase near the Chilean shoreline in the southeast Pacific due to pollution from continental sources. The effect extends ~800 to 1000 km offshore. The additional particles are mainly sulfates from anthropogenic sources, but various other particle types are present in small percentages. Sulfate internally mixed with sea-salt also occurs in and out of cloud. Smelters are apparently a smaller particle source to the VOCALS study region than previously supposed, at least along 20°S.

A variety of particle sizes down to at least 0.055 μm in diameter can act as cloud nuclei in stratocumulus clouds, not just the largest ones. The smaller nuclei are often associated with smaller droplets. This is likely due to the high supersaturations experienced by some cloud parcels, and to mixing occurring in the atmosphere and during sampling. Increased pollutants result in higher droplet number concentrations and contribute to the smaller droplet effective radii near shore. Here we return to the VOCALS hypothesis presented in the Introduction: "*The small effective radii measured from space over the SEP are primarily controlled by anthropogenic, rather than natural, aerosol production.*" In fact, droplet effective radii are smaller near shore, but this is a combined effect of anthropogenic aerosol increasing droplet number concentration

(~60% impact on r_e) and the physically thinner clouds present near shore (~40% impact on r_e). Thus, smaller droplets cannot be attributed solely to anthropogenic effects.

Based on measurements from MODIS, the net effect relative to unperturbed "clean" clouds is that cloud albedo is actually lower within ~300 km of shore. Albedo is slightly higher 500-1000 km offshore, in a transition zone where droplet concentration is slightly enhanced and changes in r_e apparently dominate over changes in liquid water path. Better knowledge of factors and feedbacks controlling liquid water path is critical to understanding and predicting aerosol indirect effects in stratocumulus clouds.

Acknowledgments. Work by lead author CT was primarily supported by the National Science Foundation under ATM-0746685. Additionally, co-authors acknowledge the following agencies/grants. MA: NERC grant NE/F018673/1; JA: NSF grant ATM-0746671; PS and SS: NSF grant 0748012, NASA grants NNX08AL05G and NNX11AI52G, NCRR grant UL1RR024979, and Fulbright-CONICYT scholarship number 15093810. Data used to derive initial conditions for the numerical model were provided by the British Atmospheric Data Centre (BADC). The rest of the observational data used in this research were provided by NCAR/EOL under sponsorship of the National Science Foundation: http://data.eol.ucar.edu/. We would like to especially thank the National Center for Atmospheric Research C-130 flight and support crew. We also thank Dr. Jefferson Snider for helpful discussions and Droplet Measurement Technologies for modification of the University of Colorado benchtop UHSAS instrument for operation under flight conditions. Any opinions, findings, and conclusions or recommendations expressed in this material are those of the authors and do not necessarily reflect the views of the National Science Foundation or other agencies cited.

References

Ackerman, A. S., Toon, O. B., Stevens, D. E., Heymsfield, A. J., Ramanathan, V., and Welton, E. J.: Reduction of tropical cloudiness by soot, Science, 288, 1042-1047, 2000.

Ackerman, A. S., Toon, O. B., Stevens, D. E., and Coakley, J. A.: Enhancement of cloud cover and suppression of nocturnal drizzle in stratocumulus polluted by haze, Geophys Res Lett, 30, Doi 10.1029/2002gl016634, 2003.

Ackerman, A. S., Kirkpatrick, M. P., Stevens, D. E., and Toon, O. B.: The impact of humidity above stratiform clouds on indirect aerosol climate forcing, Nature, 432, 1014-1017, 10.1038/nature03174, 2004.

Allen, G., Coe, H., Clarke, A., Bretherton, C., Wood, R., Abel, S. J., Barrett, P., Brown, P., George, R., Freitag, S., McNaughton, C., Howell, S., Shank, L., Kapustin, V., Brekhovskikh, V., Kleinman, L., Lee, Y. N., Springston, S., Toniazzo, T., Krejci, R., Fochesatto, J., Shaw, G., Krecl, P., Brooks, B., McMeeking, G., Bower, K. N., Williams, P. I., Crosier, J., Crawford, I., Connolly, P., Allan, J. D., Covert, D., Bandy, A. R., Russell, L. M., Trembath, J., Bart, M., McQuaid, J. B., Wang, J., and Chand, D.: South East Pacific atmospheric composition and variability sampled along 20 degrees S during VOCALS-REx, Atmos Chem Phys, 11, 5237-5262, DOI 10.5194/acp-11-5237-2011, 2011.

Anderson, J., Moore, G., Fernando, H., and Hyde, P.: A field study of particulate emissions from major roadways in the Phoenix airshed495, 101, 2006.

Anderson, J. R., Aggett, F. J., Buseck, P. R., Germani, M. S., and Shattuck, T. W.: Chemistry of Individual Aerosol Particles from Chandler, Arizona, an Arid Urban Environment, Environ Sci Technol, 22, 811-818, 1988.

Anderson, J. R., Buseck, P. R., Patterson, T. L., and Arimoto, R.: Characterization of the Bermuda tropospheric aerosol by combined individual-particle and bulk-aerosol analysis, Atmos Environ, 30, 319-338, 10.1016/1352-2310(95)00170-4, 1996.

Anderson, T. L., Charlson, R. J., and Covert, D. S.: Calibration of a counterflow virtual impactor at aerodynamic diameters from 1 to 15 micrometers, Aerosol Sci Tech, 19, 317-329, 10.1080/02786829308959639, 1993.

Andrejczuk, M., Reisner, J. M., Henson, B., Dubey, M. K., and Jeffery, C. A.: The potential impacts of pollution on a nondrizzling stratus deck: Does aerosol number matter more than type?, J Geophys Res-Atmos, 113, 10.1029/2007jd009445, 2008.

Andrejczuk, M., Grabowski, W. W., Reisner, J., and Gadian, A.: Cloud-aerosol interactions for boundary layer stratocumulus in the Lagrangian Cloud Model, J Geophys Res-Atmos, 115, 10.1029/2010jd014248, 2010.

900 Benedict, K. B., Lee, T., and Collett, J. L.: Cloud water composition over the
901 southeastern Pacific Ocean during the VOCALS regional experiment, Atmos Environ,
902 46, 104-114, 10.1016/j.atmosenv.2011.10.029, 2012.

903 Berner, A. H., Bretherton, C. S., and Wood, R.: Large-eddy simulation of mesoscale
904 dynamics and entrainment around a pocket of open cells observed in VOCALS-REx
905 RF06, Atmos Chem Phys, 11, 10525-10540, 10.5194/acp-11-10525-2011, 2011.

906 Brenguier, J. L., Pawlowska, H., Schuller, L., Preusker, R., Fischer, J., and Fouquart,
907 Y.: Radiative properties of boundary layer clouds: Droplet effective radius versus
908 number concentration, J Atmos Sci, 57, 803-821, 10.1175/1520-
909 0469(2000)057<0803:rpoblc>2.0.co;2, 2000.

910 Bretherton, C. S., Wood, R., George, R. C., Leon, D., Allen, G., and Zheng, X.:
911 Southeast Pacific stratocumulus clouds, precipitation and boundary layer structure
912 sampled along 20 degrees S during VOCALS-REx, Atmos Chem Phys, 10, 10639-
913 10654, DOI 10.5194/acp-10-10639-2010, 2010.

914 Chapman, E. G., Gustafson, W. I., Easter, R. C., Barnard, J. C., Ghan, S. J., Pekour, M.
915 S., and Fast, J. D.: Coupling aerosol-cloud-radiative processes in the WRF-Chem
916 model: Investigating the radiative impact of elevated point sources, Atmos Chem Phys,
917 9, 945-964, 2009.

918 Chuang, P. Y.: Sensitivity of cloud condensation nuclei activation processes to kinetic
919 parameters, Journal of Geophysical Research, 111, 10.1029/2005jd006529, 2006.

920 Clarke, A. D., Uehara, T., and Porter, J. N.: Atmospheric nuclei and related aerosol
921 fields over the Atlantic: Clean subsiding air and continental pollution during ASTEX,
922 Journal of Geophysical Research, 102, 25281-25292, 1997.

923 Clarke, A. D., and Kapustin, V. N.: A pacific aerosol survey. Part I: A decade of data on
924 particle production, transport, evolution, and mixing in the troposphere, J Atmos Sci, 59,
925 363-382, 10.1175/1520-0469(2002)059<0363:apaspi>2.0.co;2, 2002.

926 Comstock, K. K., Yuter, S. E., Wood, R., and Bretherton, C. S.: The three-dimensional
927 structure and kinematics of drizzling stratocumulus, Mon Weather Rev, 135, 3767-3784,
928 Doi 10.1175/2007mwr1944.1, 2007.

929 Fahey, K. M., and Pandis, S. N.: Optimizing model performance: variable size resolution
930 in cloud chemistry modeling, Atmos Environ, 35, 4471-4478, 10.1016/s1352-
931 2310(01)00224-2, 2001.

932 Fast, J. D., and Easter, R. C.: A Lagrangian Particle Dispersion Model Compatible with
933 WRF, 7th Annual WRF User's Workshop, Boulder, CO, 19-22 June 2006, 2006.

934 Fast, J. D., Gustafson, W. I., Easter, R. C., Zaveri, R. A., Barnard, J. C., Chapman, E.
935 G., Grell, G. A., and Peckham, S. E.: Evolution of ozone, particulates, and aerosol direct

936 radiative forcing in the vicinity of Houston using a fully coupled meteorology-chemistry-
937 aerosol model, J Geophys Res-Atmos, 111, 10.1029/2005jd006721, 2006.

938 Feingold, G., and Kreidenweis, S. M.: Cloud processing of aerosol as modeled by a
939 large eddy simulation with coupled microphysics and aqueous chemistry, J Geophys
940 Res-Atmos, 107, 10.1029/2002jd002054, 2002.

941 George, R. C., and Wood, R.: Subseasonal variability of low cloud radiative properties
942 over the southeast Pacific Ocean, Atmos Chem Phys, 10, 4047-4063, DOI 10.5194/acp-
943 10-4047-2010, 2010.

944 Grell, G. A., Peckham, S. E., Schmitz, R., McKeen, S. A., Frost, G., Skamarock, W. C.,
945 and Eder, B.: Fully coupled "online" chemistry within the WRF model, Atmos Environ,
946 39, 6957-6975, 10.1016/j.atmosenv.2005.04.027, 2005.

947 Hartmann, D. L., Ockertbell, M. E., and Michelsen, M. L.: THE EFFECT OF CLOUD
948 TYPE ON EARTHS ENERGY-BALANCE - GLOBAL ANALYSIS, J Climate, 5, 1281-
949 1304, 10.1175/1520-0442(1992)005<1281:teocto>2.0.co;2, 1992.

950 Hawkins, L. N., Russell, L. M., Covert, D. S., Quinn, P. K., and Bates, T. S.: Carboxylic
951 acids, sulfates, and organosulfates in processed continental organic aerosol over the
952 southeast Pacific Ocean during VOCALS-REx 2008, J Geophys Res-Atmos, 115, Artn
953 D13201, Doi 10.1029/2009jd013276, 2010.

954 Hegg, D. A., and Hobbs, P. V.: The homogeneous oxidation of sulfur dioxide in cloud
955 droplets, Atmos Environ, 13, 981-987, 1979.

956 Hegg, D. A., Covert, D. S., Jonsson, H. H., and Woods, R. K.: A simple relationship
957 between cloud drop number concentration and precursor aerosol concentration for the
958 regions of Earth's large marine stratocumulus decks, Atmos Chem Phys, 12, 1229-
959 1238, 10.5194/acp-12-1229-2012, 2012.

960 Hudson, J. G., and Frisbie, P. R.: CLOUD CONDENSATION NUCLEI NEAR MARINE
961 STRATUS, J Geophys Res-Atmos, 96, 20795-20808, 10.1029/91jd02212, 1991.

962 Hudson, J. G.: Variability of the relationship between particle size and cloud-nucleating
963 ability, Geophys Res Lett, 34, 10.1029/2006gl028850, 2007.

964 Huneeus, N., Gallardo, L., and Rutllant, J. A.: Offshore transport episodes of
965 anthropogenic sulfur in northern Chile: Potential impact on the stratocumulus cloud
966 deck, Geophys Res Lett, 33, Artn L19819
967 Doi 10.1029/2006gl026921, 2006.

968 Jiang, H. L., Feingold, G., and Cotton, W. R.: Simulations of aerosol-cloud-dynamical
969 feedbacks resulting from entrainment of aerosol into the marine boundary layer during
970 the Atlantic Stratocumulus Transition Experiment, J Geophys Res-Atmos, 107,
971 10.1029/2001jd001502, 2002.

King, M. D., and Harshvardhan: Comparative Accuracy of Selected Multiple-Scattering Approximations, J Atmos Sci, 43, 784-801, 1986.

Kleinman, L. I., Daum, P. H., Lee, Y. N., Lewis, E. R., Sedlacek, A. J., Senum, G. I., Springston, S. R., Wang, J., Hubbe, J., Jayne, J., Min, Q., Yum, S. S., and Allen, G.: Aerosol concentration and size distribution measured below, in, and above cloud from the DOE G-1 during VOCALS-REx, Atmospheric Chemistry and Physics Discussions, 11, 17289-17336, 10.5194/acpd-11-17289-2011, 2011.

Kulkarni, G., and Twohy, C.: Computational fluid dynamics studies to understand ice crystal and liquid droplet breakup within an airborne counterflow virtual impactor, Thirtieth Annual Conference, American Association for Aerosol Research,, Orlando, FL, October 3-7 2011, 2011.

Lance, S., Brock, C. A., Rogers, D., and Gordon, J. A.: Water droplet calibration of the Cloud Droplet Probe (CDP) and in-flight performance in liquid, ice and mixed-phase clouds during ARCPAC, Atmospheric Measurement Techniques, 3, 1683-1706, 10.5194/amt-3-1683-2010, 2010.

Leaitch, W. R., Banic, C. M., Isaac, G. A., Couture, M. D., Liu, P. S. K., Gultepe, I., Li, S. M., Kleinman, L., Daum, P. H., and MacPherson, J. I.: Physical and chemical observations in marine stratus during the 1993 North Atlantic Regional Experiment: Factors controlling cloud droplet number concentrations, J Geophys Res-Atmos, 101, 29123-29135, 10.1029/96jd01228, 1996.

Lee, S. S., Penner, J. E., and Saleeby, S. M.: Aerosol effects on liquid-water path of thin stratocumulus clouds, J Geophys Res-Atmos, 114, Artn D07204 Doi 10.1029/2008jd010513, 2009.

Lu, C. S., Liu, Y. G., and Niu, S. J.: Examination of turbulent entrainment-mixing mechanisms using a combined approach, J Geophys Res-Atmos, 116, 10.1029/2011jd015944, 2011.

Marshak, A., Wen, G., Coakley, J. A., Remer, L. A., Loeb, N. G., and Cahalan, R. F.: A simple model for the cloud adjacency effect and the apparent bluing of aerosols near clouds, J Geophys Res-Atmos, 113, Artn D14s17 Doi 10.1029/2007jd009196, 2008.

Noone, K. J., Ogren, J. A., Heintzenberg, J., Charlson, R. J., and Covert, D. S.: DESIGN AND CALIBRATION OF A COUNTERFLOW VIRTUAL IMPACTOR FOR SAMPLING OF ATMOSPHERIC FOG AND CLOUD DROPLETS, Aerosol Sci Tech, 8, 235-244, 10.1080/02786828808959186, 1988.

Ogren, J. A., and Charlson, R. J.: Implications for models and measurements of chemical inhomogeneities among cloud droplets, Tellus B, 44B, 208-225., 1992.

Ostrom, E., Noone, K. J., and Pockalny, R. A.: Cloud droplet residual particle microphysics in marine stratocumulus clouds observed during the Monterey Area Ship

1010 Track experiment, J Atmos Sci, 57, 2671-2683, 10.1175/1520-
1011 0469(2000)057<2671:cdrpmi>2.0.co;2, 2000.

1012 Painemal, D., and Zuidema, P.: Microphysical variability in southeast Pacific
1013 Stratocumulus clouds: synoptic conditions and radiative response, Atmos Chem Phys,
1014 10, 6255-6269, DOI 10.5194/acp-10-6255-2010, 2010.

1015 Reisner, J. M., Mousseau, V. A., Wyszogrodzki, A. A., and Knoll, D. A.: An implicitly
1016 balanced hurricane model with physics-based preconditioning, Mon Weather Rev, 133,
1017 1003-1022, 10.1175/mwr2901.1, 2005.

1018 Saide, P. E., Spak, S. N., Carmichael, G. R., Mena-Carrasco, M. A., Yang, Q., Howell,
1019 S., Leon, D. C., Snider, J. R., Bandy, A. R., Collett, J. L., Benedict, K. B., de Szoeke, S.
1020 P., Hawkins, L. N., Allen, G., Crawford, I., Crosier, J., and Springston, S. R.: Evaluating
1021 WRF-Chem aerosol indirect effects in Southeast Pacific marine stratocumulus during
1022 VOCALS-REx, Atmos Chem Phys, 12, 3045-3064, 10.5194/acp-12-3045-2012, 2012.

1023 Saide, P. E., Carmichael, G., Spak, S. N., Minnis, P., and Ayers, J. K.: Improving
1024 aerosol distributions below clouds by assimilating satellite-retrieved cloud droplet
1025 number, P Natl Acad Sci USA, in press.

1026 Schüller, M., Estrada, A., and Bringezu, S.: Mapping Environmental Performance of
1027 International Raw Material Production Flows: a Comparative Case Study for the Copper
1028 Industry of Chile and Germany, Minerals and Energy, 2, 29-45, 2008.

1029 Shank, L. M., Howell, S., Clarke, A. D., Freitag, S., Brekhovskikh, V., Kapustin, V.,
1030 McNaughton, C., Campos, T., and Wood, R.: Organic matter and non-refractory aerosol
1031 over the remote Southeast Pacific: oceanic and combustion sources, Atmos Chem
1032 Phys, 12, 557-576, 10.5194/acp-12-557-2012, 2012.

1033 Silva, P., Liu, D.-Y., Noble, C. A., and Prather, K. A.: Size and chemical characterization
1034 of individual particles resulting from biomass burning of local southern California
1035 species, Environ Sci Technol, 33, 3068-3076, 1999.

1036 Skamarock, W. C., Klemp, J. B., Dudhia, J., Gill, D. O., Barker, D. M., Duda, M. G.,
1037 Huang, X.-Y., Wang, W., and Powers, J. G.: A Description of the Advanced Research
1038 WRF, Version 3, Technical Report NCAR/TN475+ST Boulder, CO, 2008.

1039 Snider, J. R., and Brenguier, J. L.: Cloud condensation nuclei and cloud droplet
1040 measurements during ACE-2. , Tellus B, 52, 828-842, 2000.

1041 Solomon, S., Qin, D., Manning, M., Marquis, M., Averyt, K., Tignor, M. M. B., Jr., H. L.
1042 M., and Chen, Z.: Climate Change 2007: Working Group I: The Physical Science Basis,
1043 Intergovernmental Panel on Climate Change, 996, 2007.

1044 Spak, S. N., Mena-Carrasco, M. A., and Carmichael, G. R.: Atmospheric transport of
1045 anthropogenic oxidized sulfur over the Southeast Pacific during VOCALS REx, CLIVAR
1046 Exchanges, 53, 20-21, 2010.

1047 Stephens, G. L.: Radiation Profiles in Extended Water Clouds .2. Parameterization
1048 Schemes, J Atmos Sci, 35, 2123-2132, 1978.

1049 Stevens, B., Moeng, C. H., Ackerman, A. S., Bretherton, C. S., Chlond, A., De Roode,
1050 S., Edwards, J., Golaz, J. C., Jiang, H. L., Khairoutdinov, M., Kirkpatrick, M. P.,
1051 Lewellen, D. C., Lock, A., Muller, F., Stevens, D. E., Whelan, E., and Zhu, P.:
1052 Evaluation of large-Eddy simulations via observations of nocturnal marine
1053 stratocumulus, Mon Weather Rev, 133, 1443-1462, 10.1175/mwr2930.1, 2005a.

1054 Stevens, B., Vali, G., Comstock, K., Wood, R., van Zanten, M. C., Austin, P. H.,
1055 Bretherton, C. S., and Lenschow, D. H.: Pockets of open cells and drizzle in marine
1056 stratocumulus, B Am Meteorol Soc, 86, 51-+, Doi 10.1175/Bams-86-1-51, 2005b.

1057 Stevens, B., and Feingold, G.: Untangling aerosol effects on clouds and precipitation in
1058 a buffered system, Nature, 461, 607-613, Doi 10.1038/Nature08281, 2009.

1059 Stohl, A., Forster, C., Frank, A., Seibert, P., and Wotawa, G.: Technical Note : The
1060 Lagrangian particle dispersion model FLEXPART version 6.2, Atmos Chem Phys, 5,
1061 2461-2474, 2005.

1062 Toniazzo, T., Abel, S. J., Wood, R., Mechoso, C. R., Allen, G., and Shaffrey, L. C.:
1063 Large-scale and synoptic meteorology in the south-east Pacific during the observations
1064 campaign VOCALS-REx in austral Spring 2008, Atmos Chem Phys, 11, 4977-5009,
1065 DOI 10.5194/acp-11-4977-2011, 2011.

1066 Tsapakis, M., Lagoudaki, E., Stephanou, E. G., Kavouras, I. G., Koutrakis, P., Oyola, P.,
1067 and von Baer, D.: The composition and sources of PM2.5 organic aerosol in two urban
1068 areas of Chile, Atmos Environ, 36, 3851-3863, 10.1016/s1352-2310(02)00269-8, 2002.

1069 Twohy, C. H., Austin, P. H., and Charlson, R. J.: Chemical consequences of the initial
1070 diffusional growth of cloud droplets: a clean marine case, Tellus B, 41, 51-60, DOI
1071 10.1111/j.1600-0889.1989.tb00124.x, 1989a.

1072 Twohy, C. H., Clarke, A. D., Warren, S. G., Radke, L. F., and Charlson, R. J.: Light-
1073 Absorbing Material Extracted from Cloud Droplets and Its Effect on Cloud Albedo, J
1074 Geophys Res-Atmos, 94, 8623-8631, 1989b.

1075 Twohy, C. H., and Hudson, J. G.: Measurements of Cloud Condensation Nuclei Spectra
1076 within Maritime Cumulus Cloud Droplets - Implications for Mixing Processes, J Appl
1077 Meteorol, 34, 815-833, 1995.

1078 Twohy, C. H., Schanot, A. J., and Cooper, W. A.: Measurement of condensed water
1079 content in liquid and ice clouds using an airborne counterflow virtual impactor, J Atmos
1080 Ocean Tech, 14, 197-202, 1997.

1081 Twohy, C. H., Strapp, J. W., and Wendisch, M.: Performance of a counterflow virtual
1082 impactor in the NASA Icing Research Tunnel, J Atmos Ocean Tech, 20, 781-790, 2003.

1083 Twohy, C. H., Petters, M. D., Snider, J. R., Stevens, B., Tahnk, W., Wetzel, M., Russell,
1084 L., and Burnet, F.: Evaluation of the aerosol indirect effect in marine stratocumulus
1085 clouds: Droplet number, size, liquid water path, and radiative impact, J Geophys Res-
1086 Atmos, 110, Artn D08203
1087 Doi 10.1029/2004jd005116, 2005.

1088 Twohy, C. H., Coakley, J. A., and Tahnk, W. R.: Effect of changes in relative humidity
1089 on aerosol scattering near clouds, J Geophys Res-Atmos, 114, Artn D05205
1090 Doi 10.1029/2008jd010991, 2009.

1091 Twomey, S.: Pollution and Planetary Albedo, Atmos Environ, 8, 1251-1256, 1974.

1092 Wallace, J. M., and Hobbs, P. V.: Atmospheric Science: An Introductory Survey.,
1093 Academic Press, 467 pp., 1977.

1094 Wang, Z., French, J., Vali, G., Wechsler, P., Haimov, S., Rodi, A., Deng, M., Leon, D.,
1095 Snider, J., Peng, L., and Pazmany, A. L.: Single Aircraft Integration of Remote Sensing
1096 and In Situ Sampling for the Study of Cloud Microphysics and Dynamics, B Am
1097 Meteorol Soc, 93, 653-668, 10.1175/bams-d-11-00044.1, 2012.

1098 Weber, R. J., Clarke, A. D., Litchy, M., Li, J., Kok, G., Schillawski, R. D., and McMurry,
1099 P.: Spurious aerosol measurements when sampling from aircraft in the vicinity of
1100 clouds, Journal of Geophysical Research, 103, 28337-28346, 1998.

1101 Wood, R., Bretherton, C. S., and Hartmann, D. L.: Diurnal cycle of liquid water path over
1102 the subtropical and tropical oceans, Geophys Res Lett, 29, Artn 2092
1103 Doi 10.1029/2002gl015371, 2002.

1104 Wood, R.: Cancellation of aerosol indirect effects in marine stratocumulus through cloud
1105 thinning, J Atmos Sci, 64, 2657-2669, 10.1175/jas3942.1, 2007.

1106 Wood, R., Bretherton, C. S., Leon, D., Clarke, A. D., Zuidema, P., Allen, G., and Coe,
1107 H.: An aircraft case study of the spatial transition from closed to open mesoscale
1108 cellular convection over the Southeast Pacific, Atmos Chem Phys, 11, 2341-2370,
1109 10.5194/acp-11-2341-2011, 2011a.

1110 Wood, R., Mechoso, C. R., Bretherton, C. S., Weller, R. A., Huebert, B., Straneo, F.,
1111 Albrecht, B. A., Coe, H., Allen, G., Vaughan, G., Daum, P., Fairall, C., Chand, D.,
1112 Klenner, L. G., Garreaud, R., Grados, C., Covert, D. S., Bates, T. S., Krejci, R., Russell,
1113 L. M., de Szoeke, S., Brewer, A., Yuter, S. E., Springston, S. R., Chaigneau, A.,
1114 Toniazzo, T., Minnis, P., Palikonda, R., Abel, S. J., Brown, W. O. J., Williams, S.,
1115 Fochesatto, J., Brioude, J., and Bower, K. N.: The VAMOS Ocean-Cloud-Atmosphere-
1116 Land Study Regional Experiment (VOCALS-REx): goals, platforms, and field
1117 operations, Atmos Chem Phys, 11, 627-654, DOI 10.5194/acp-11-627-2011, 2011b.

1118 Wyant, M. C., Wood, R., Bretherton, C. S., Mechoso, C. R., Bacmeister, J., Balmaseda,
1119 M. A., Barrett, B., Codron, F., Earnshaw, P., Fast, J., Hannay, C., Kaiser, J. W.,
1120 Kitagawa, H., Klein, S. A., Kohler, M., Manganello, J., Pan, H. L., Sun, F., Wang, S.,

and Wang, Y.: The PreVOCA experiment: modeling the lower troposphere in the Southeast Pacific, Atmos Chem Phys, 10, 4757-4774, DOI 10.5194/acp-10-4757-2010, 2010.

Yang, M., Huebert, B. J., Blomquist, B. W., Howell, S. G., Shank, L. M., McNaughton, C. S., Clarke, A. D., Hawkins, L. N., Russell, L. M., Covert, D. S., Coffman, D. J., Bates, T. S., Quinn, P. K., Zagorac, N., Bandy, A. R., de Szoeke, S. P., Zuidema, P. D., Tucker, S. C., Brewer, W. A., Benedict, K. B., and Collett, J. L.: Atmospheric sulfur cycling in the southeastern Pacific - longitudinal distribution, vertical profile, and diel variability observed during VOCALS-REx, Atmos Chem Phys, 11, 5079-5097, DOI 10.5194/acp-11-5079-2011, 2011a.

Yang, Q., W. I. Gustafson, J., Fast, J. D., Wang, H., Easter, R. C., Morrison, H., Lee, Y. N., Chapman, E. G., Spak, S. N., and Mena-Carrasco, M. A.: Assessing regional scale predictions of aerosols, marine stratocumulus, and their interactions during VOCALS-REx using WRF-Chem, Atmos Chem Phys, 11, 11951-11975, 10.5194/acp-11-11951-2011, 2011b.

Yang, Q., Gustafson Jr, W. I., Fast, J. D., Wang, H., Easter, R. C., Wang, M., Ghan, S. J., Berg, L. K., Leung, L. R., and Morrison, H.: Impact of natural and anthropogenic aerosols on stratocumulus and precipitation in the Southeast Pacific: a regional modelling study using WRF-Chem, Atmos. Chem. Phys. Discuss., 12, 14623-14667, 10.5194/acpd-12-14623-2012, 2012.

Zaveri, R. A., and Peters, L. K.: A new lumped structure photochemical mechanism for large-scale applications, J Geophys Res-Atmos, 104, 30387-30415, 10.1029/1999jd900876, 1999.

Zaveri, R. A., Easter, R. C., Fast, J. D., and Peters, L. K.: Model for Simulating Aerosol Interactions and Chemistry (MOSAIC), J Geophys Res-Atmos, 113, 10.1029/2007jd008782, 2008.

Zheng, X., Albrecht, B., Jonsson, H. H., Khelif, D., Feingold, G., Minnis, P., Ayers, K., Chuang, P., Donaher, S., Rossiter, D., Ghate, V., Ruiz-Plancarte, J., and Sun-Mack, S.: Observations of the boundary layer, cloud, and aerosol variability in the southeast Pacific near-coastal marine stratocumulus during VOCALS-REx, Atmos Chem Phys, 11, 9943-9959, DOI 10.5194/acp-11-9943-2011, 2011.

Zuidema, P., Leon, D., Pazmany, A., and Cadeddu, M.: Aircraft millimeter-wave retrievals of cloud liquid water path and water vapor during VOCALS-REx, Atmos Chem Phys, 12, 355-369, 10.5194/acp-12-355-2012, 2012.

1157 Significance of Fitted Relationships between Various Parameters

Parameters (Y vs X)	r^2 [a]	r [b]	n [c]	t_{obs} [d]	t_{crit} [e]	*Reject?* [f]	*Regression Equation*
N_p (> 0.055 μm) vs Dist	0.57	(-)0.75	39	7.00	1.68	Yes	Y =1389-397.5log(X)
N_p (> 0.1 μm) vs Dist	0.61	(-)0.78	39	7.61	1.68	Yes	Y =1021-294.4log(X)
N_p (> 0.01 μm) vs Dist	0.01	(-)0.10	39	0.61	1.68	No	
N_d vs Dist	0.57	(-)0.75	39	7.00	1.68	Yes	Y =556.8-151.7log(X)
N_p (> 0.055 μm) vs N_d (log fit)	0.56	(+)0.75	39	6.86	1.68	Yes	Y =-318.8+190.5log(X)
N_p (> 0.1 μm) vs N_d (log fit)	0.57	(+)0.75	39	7.00	1.68	Yes	Y =-296.5+193.2log(X)
Mean drop diam vs Dist	0.39	(+)0.62	39	4.86	1.68	Yes	Y =-8.5+8.101log(x)
r_e vs Dist	0.37	(+)0.61	39	4.66	1.68	Yes	Y =-3.7+4.104log(X)
Drizzle Conc vs Dist	0.08	(+)0.28	39	1.79	1.68	Yes	Y =-77+34.9log(X)
Mean Drizzle Diam vs Dist	0.37	(+)0.61	39	4.66	1.68	Yes	Y =-76+56.96log(X)
Cloud Thickness vs Dist	0.27	(+)0.52	27	3.04	1.70	Yes	Y =-136+162.3log(X)
LWP vs Dist	0.22	(+)0.47	39	3.23	1.68	Yes	Y --237+115.9log(X)
Cloud albedo vs Dist (in situ day)	0.11	(+)0.33	21	1.52	1.68	No	
Cloud albedo vs Dist (in-situ night)	0.03	(+)0.17	18	0.69	1.68	No	
Cloud Albedo vs Dist MODIS (poly fit)	0.83	0.91	15	7.33	1.68	Yes	$Y=0.339+0.000546225X-5.200984\times10^{-7}X^2+1.377992\times10^{-10}X^3$

1158 Parameter Description: Dist = distance west from shore along 20°S, N_p = particle concentration, N_d=droplet concentration from
1159 CDP probe, other droplet parameters are also from the CDP probe, drizzle parameters from the 2D-C probe, cloud thickness,
1160 LWP and albedo as described in Sect. 3.4.
1161 a) Pearson coefficient of determination from the appropriate figure/regression.
1162 b) Pearson coefficient of correlation. Also denotes sign of relationship (positive or negative) for linear or logarithmic fit.
1163 c) Number of samples.
1164 d) Observed t value = $r((df)/(1-r^2))^{0.5}$. df = degrees of freedom (n-2 except for MODIS albedo when it is n-4 due to 3rd order fit).
1165 e) Critical t value at p=0.05, from statistical tables.
1166 f) If $t_{obs}>t_{crit}$, null hypothesis may be rejected.

Figure Captions

Fig. 1. a. Below-cloud aerosol number concentration vs. distance west from shore along 20°S latitude line for legs on eight different VOCALS C-130 flights. Top axis shows longitude. Green represents data from the UHSAS (>0.055 μm diameter) and purple from the PCASP (>0.10 μm) **b.** Below-cloud number concentration from the CVI CPC (>0.01 μm**) c.** Cloud droplet number concentration from the CDP as a function of distance from shore. **d.** Particle concentration in two different size ranges vs droplet concentration.

Fig. 2 a. Cloud droplet mean diameter and effective radius vs. distance west from shore. **b.** Drizzle drop mean size and number concentration as a function of distance from shore. Mean sizes below the effective detection limit of the probe (60 μm) are due to inclusion of zero values when no drizzle was present in cloud.

Fig. 3. Examples of particle types found when sampling from the C-130 during VOCALS. a) ammonium sulfate, b) biomass burning type, c) soot carbon from combustion.

Fig. 4. Particle types by number as determined by SEM/X-ray analysis for near-shore samples on 21 Oct 2008 (06:49:50 to 06:59:45 UTC)--plots a) and b), and on 24 Oct 2008 (13:41:25-13:46:40 UTC)--plots c) and d). Pie charts on left are for smaller particles approximately 0.1 to 0.2 μm in diameter, and on right, for particles larger than 0.2 μm. 1000 particles were analyzed for each sample. “Reacted sea-salt” refers to sea-salt where chlorine has been partially or completely replaced with sulfate, while “other” category may include soil-dust, organics, black carbon, or industrial material.

Fig. 5. Forward trajectories starting at major smelters that could potentially affect the VOCALS region. Trajectories are 5 days long during the VOCALS intensive period, starting every 5 days. Markers are plotted every 6 hours. Smelter locations are color coded by sulfur emissions in Gg/yr.

Fig. 6. % change in particle number concentration predicted by WRF-Chem with and without smelter emissions included. Particle size range was matched to the PCASP probe, 0.12 to 3.0 μm in diameter. Major smelters are shown as circles with A: Chuquicamata, B: Ilo, C: Caletones and D: Potrerillos.

Fig. 7. a) Comparison of aerosol number concentration between 0.12 and 3.0 μm as observed from the C-130 (blue) vs. WRF-Chem model results with smelter emissions (red) and without smelter emissions (black) for the 15 Oct 2008 to 24 Oct 2008 time period. Data are gridded into 2.5 degree longitudinal zones between 22°S and 18°S. The number of profiles is indicated at the top of each longitude bin. b) Same but for measured (Allen et al., 2011) and modeled sulfate mass between 0.04 μm to 0.625 μm, with sampling time in minutes in each longitude bin indicated at the top. For each zone, center solid (dashed) lines indicate the median (mean), and boxes indicate upper and lower quartiles with upper and lower decile whiskers.

Fig. 8. Size distributions of droplet residual nuclei from droplets larger than different diameters as noted on the top of plots. Mean residual particle size is shown at bottom of plots. Top plot is from C-130 flight 3 (21 Oct 2008) and bottom is from flight 4 (21 Oct 2008).

Fig. 9. Statistics of UHSAS geometric mean diameter for 20 pairs of below-cloud aerosol particles (blue) and CVI droplet residual nuclei (red) in VOCALS clouds with drizzle < 5 lit^{-1} and ratio of CVI total number concentration to droplet number concentration <1. Seventeen above-cloud samples are also shown in grey. The box limits represent the upper and lower quartiles, with the median as a horizontal line. The lines extending from the top and bottom of each box mark the maximum and minimum values within the data set that are within the upper quartile + (1.5 x the interquartile distance) or less than the lower quartile - (1.5 x the interquartile distance), respectively. Outliers are marked with circles.

Fig 10. UHSAS particle size distributions for four sets of paired below-cloud (blue) and in-cloud droplets (red) CVI samples in clouds with drizzle < 5 lit^{-1} and ratio of CVI total number concentration to droplet number concentration between 0.72 and 0.94. C-130 flights and in-cloud UTC times are a) flight 2: 13:33:32-13:36:58, b) flight 3: 7:18:25-7:24:40, c) flight 3: 13:14:15-13:16:40, and d) flight 11: 16:42:42-16:47:22. In-cloud distributions are less noisy than below-cloud distributions due to the enhancement factor in the CVI inlet.

Fig. 11: Probability plot of vertical velocity (1 Hz) measured along the flight track for in-cloud samples a) through d) shown in Fig. 10.

Fig. 12. Particles larger than 0.055 μm for HIGH (a,b) and LOW (c,d) Lagrangian cloud model cases after 2 hours (top) and 8 hours (bottom) of run time. Analogous to Fig. 10, the blue line shows the aerosol size distribution below the cloud, averaged between 100-350 m in height, while the red line represents the particles only present within droplets larger than 8 μm in size. The green line shows all particles within the cloud layer, including both interstitial and in-cloud particles. In-cloud was defined as points with $q_c > 10^{-6}$ g kg^{-1}.

Fig. 13. Total aerosol concentration (ambient, interstitial and within droplets) predicted by the LCM after 2 hours (top, plots a and c) and 8 hours (bottom, plots b and d), as a function of height, scaled to the top of the cloud. HIGH aerosol case results are on the left and LOW aerosol case results are on the right.

Fig 14. a. Cloud geometric thickness and liquid water path (LWP) as a function of distance west from shore along 20°S. Thickness is from the in-situ radar and lidar, while LWP uses both GVR and radar data. **b.** Top of cloud albedo vs. distance from shore calculated as described in the text (using 10:30 local values for solar zenith angle). Circles are values derived from onboard remote sensors during daytime (purple) and night-time (blue) C-130 flight segments, while red squares are derived from the MODIS

10:30 local overpass averaged over the entire VOCALS 31-day time period. Vertical bars represent one sigma variability in the MODIS data.

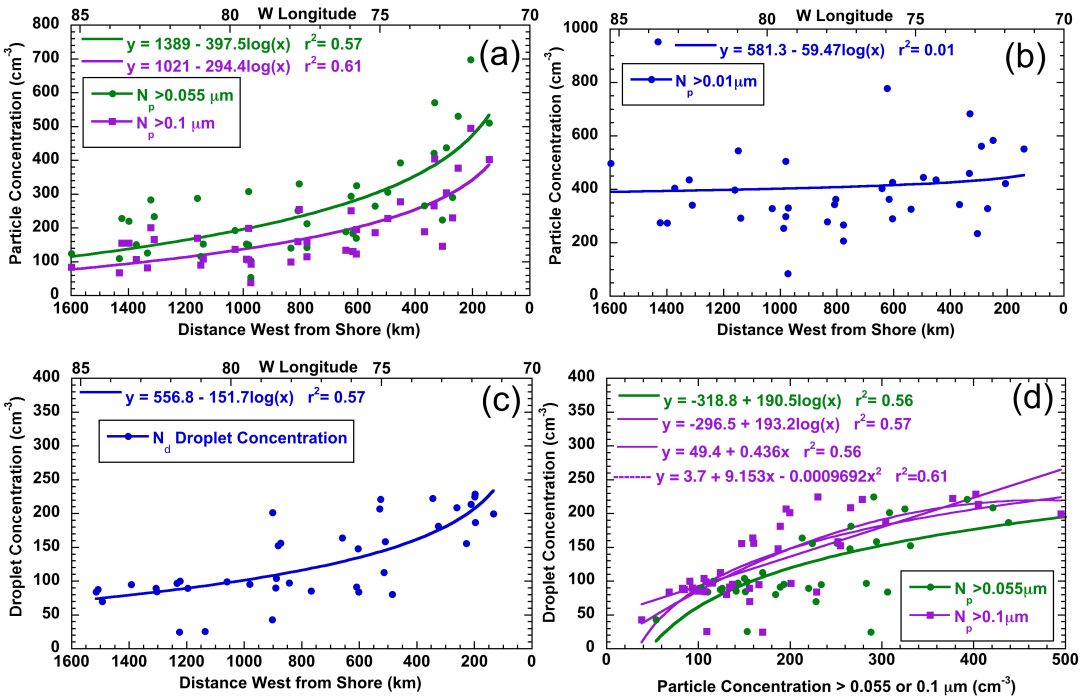

Fig. 1. a. Below-cloud aerosol number concentration vs. distance west from shore along 20°S latitude line for legs on eight different VOCALS C-130 flights. Top axis shows longitude. Green represents data from the UHSAS (>0.055 μm diameter) and purple from the PCASP (>0.10 μm) **b.** Below-cloud number concentration from the CVI CPC (>0.01 μm**) c.** Cloud droplet number concentration from the CDP as a function of distance from shore. **d.** Particle concentration in two different size ranges vs droplet concentration.

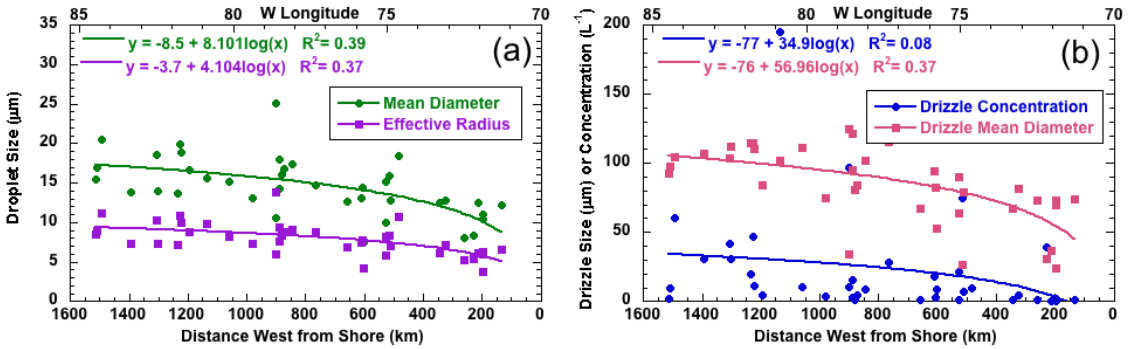

Fig. 2 a. Cloud droplet mean diameter and effective radius vs. distance west from shore. **b.** Drizzle drop mean size and number concentration as a function of distance from shore. Mean sizes below the effective detection limit of the probe (60 µm) are due to inclusion of zero values when no drizzle was present in cloud.

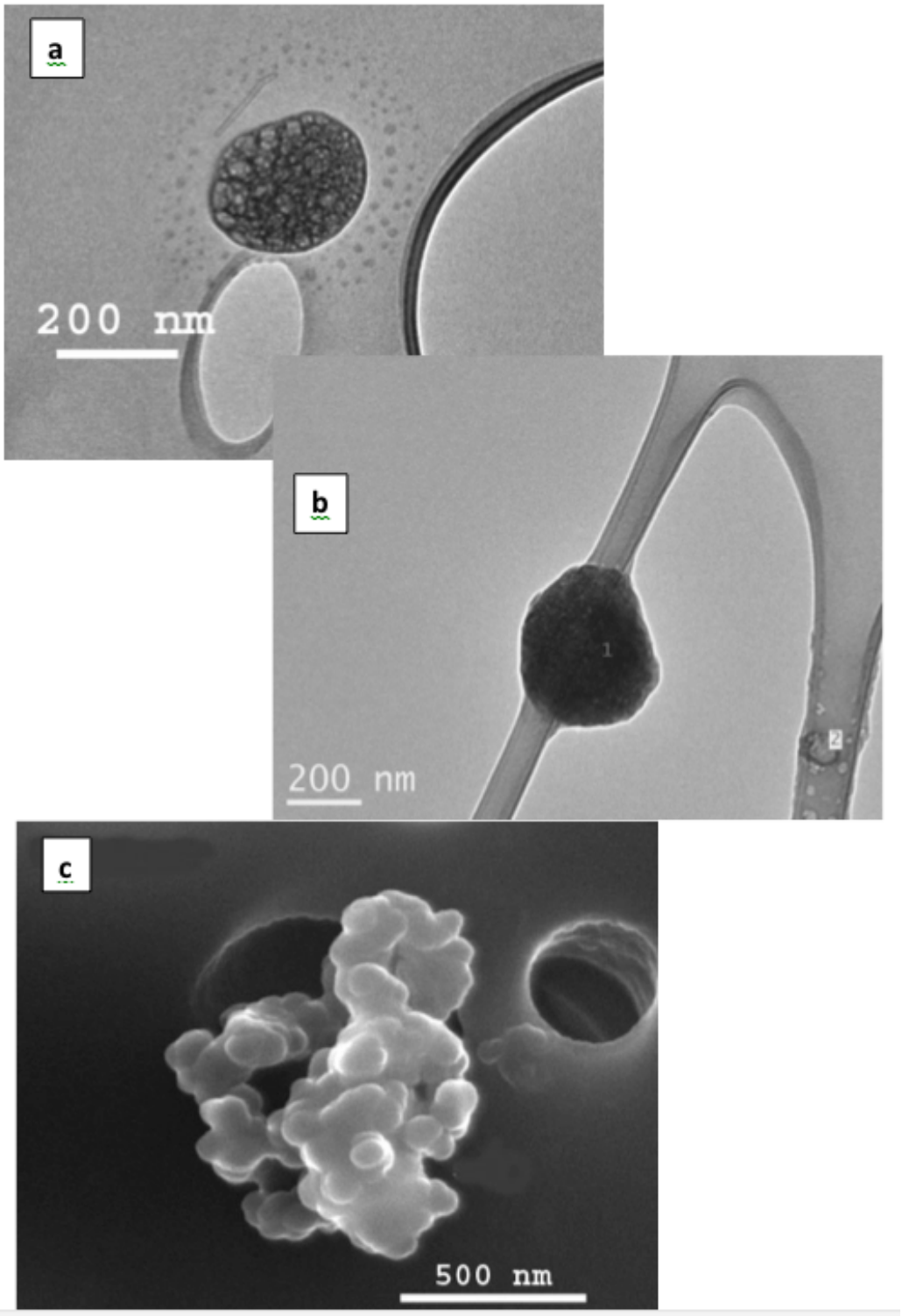

Fig. 3. Examples of particle types found when sampling from the C-130 during VOCALS. a) ammonium sulfate, b) biomass burning type, c) soot carbon from combustion.

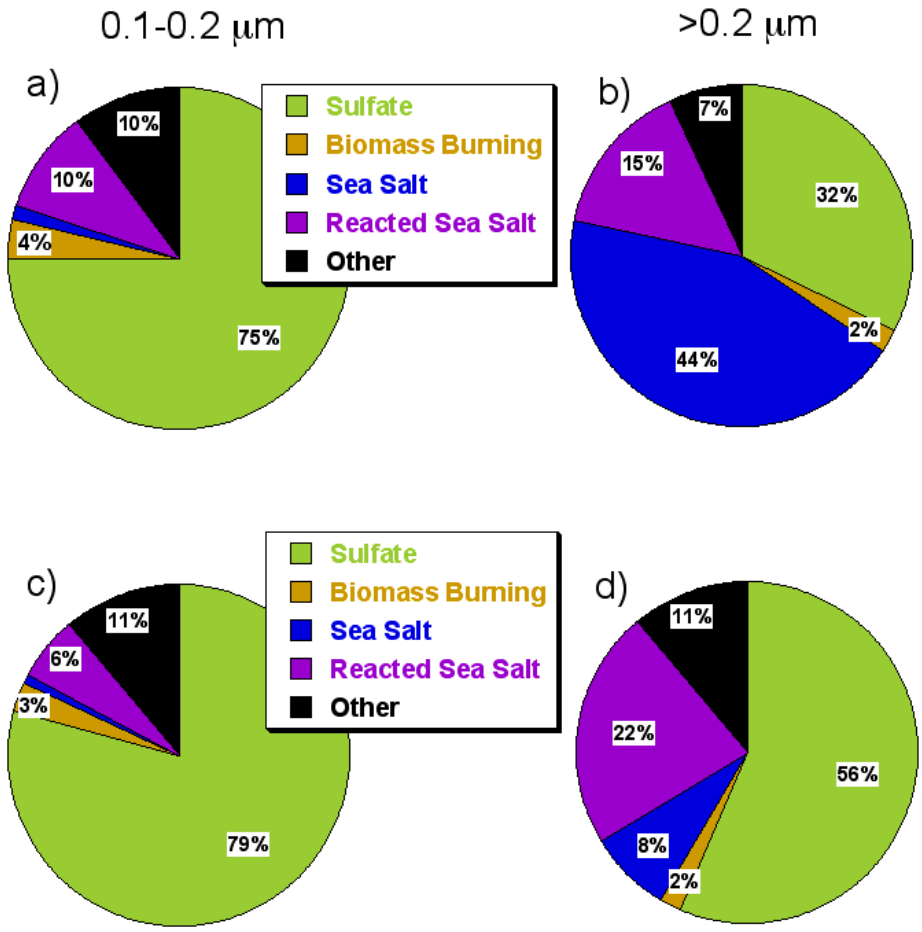

Fig. 4. Particle types by number as determined by SEM/X-ray analysis for near-shore samples on 21 Oct 2008 (06:49:50 to 06:59:45 UTC)--plots a) and b), and on 24 Oct 2008 (13:41:25-13:46:40 UTC)--plots c) and d). Pie charts on left are for smaller particles approximately 0.1 to 0.2 µm in diameter, and on right, for particles larger than 0.2 µm. 1000 particles were analyzed for each sample. “Reacted sea-salt” refers to sea-salt where chlorine has been partially or completely replaced with sulfate, while “other” category may include soil-dust, organics, black carbon, or industrial material.

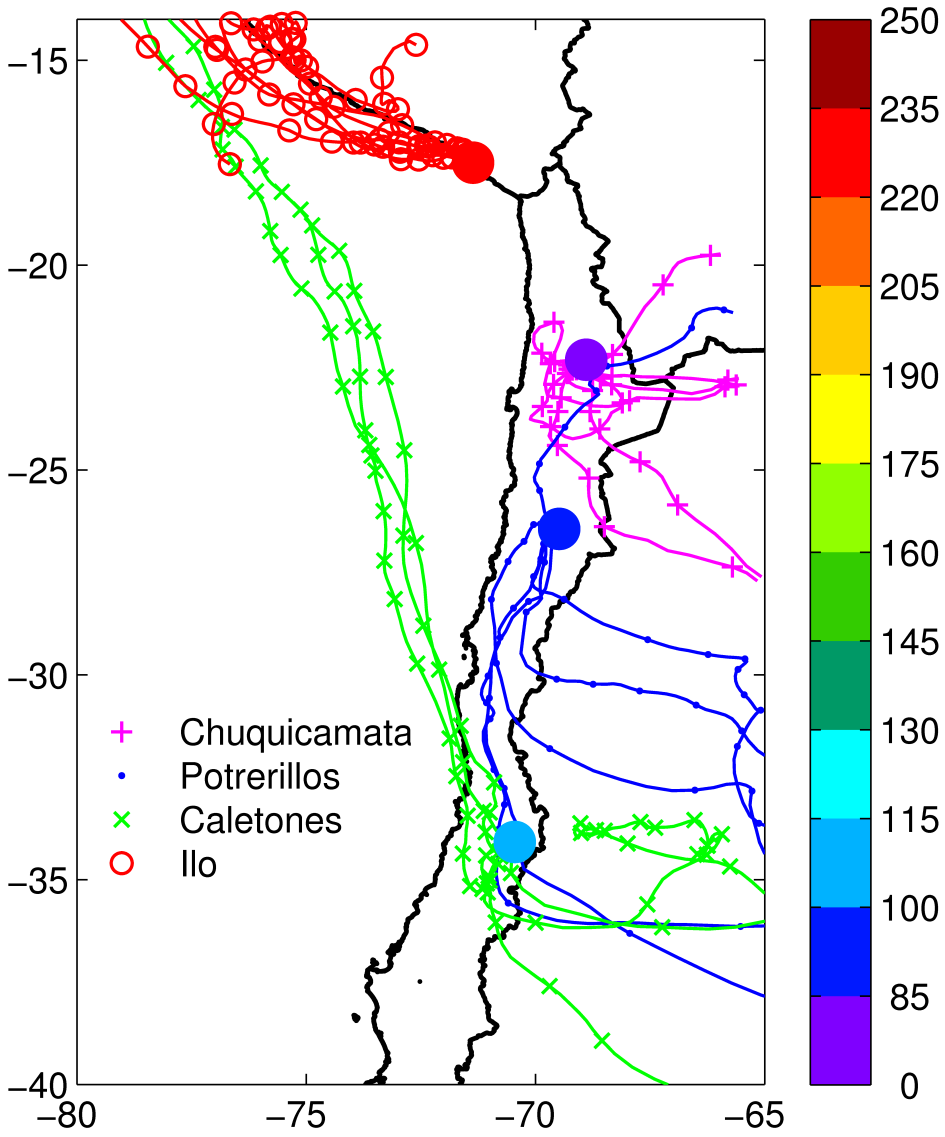

Fig. 5. Forward trajectories starting at major smelters that could potentially affect the VOCALS region. Trajectories are 5 days long during the VOCALS intensive period, starting every 5 days. Markers are plotted every 6 hours. Smelter locations are color coded by sulfur emissions in Gg/yr.

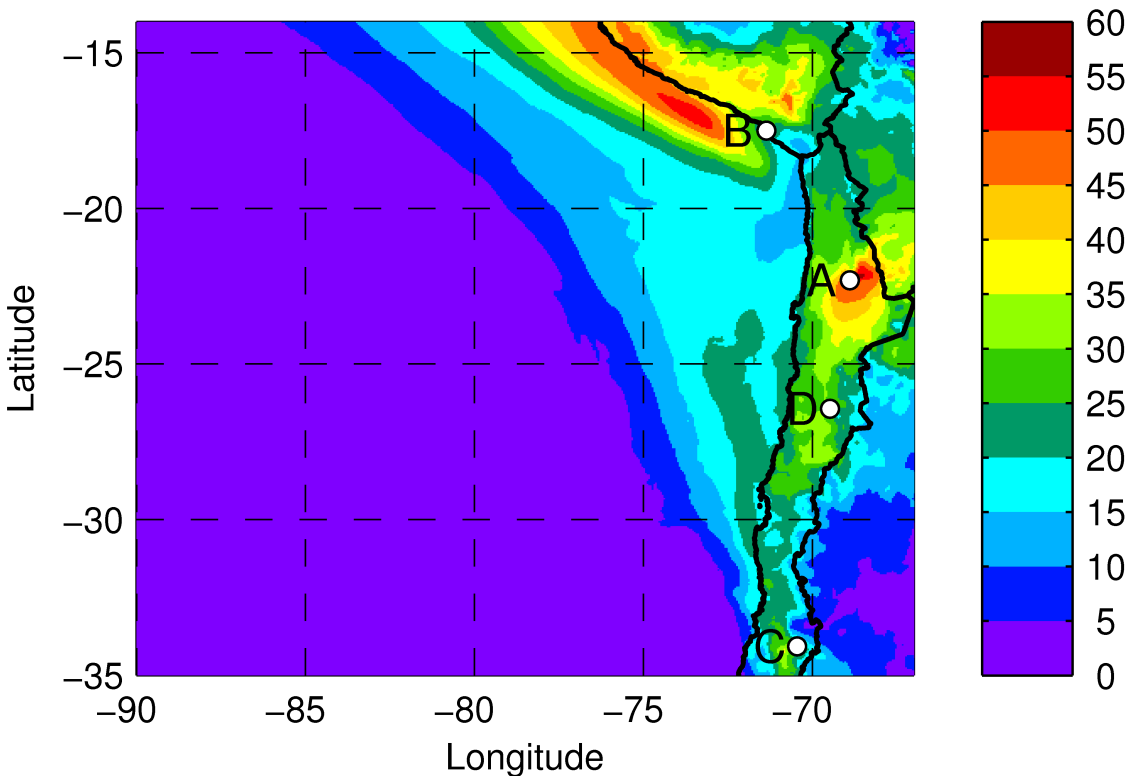

Fig. 6. % change in particle number concentration predicted by WRF-Chem with and without smelter emissions included. Particle size range was matched to the PCASP probe, 0.12 to 3.0 μm in diameter. Major smelters are shown as circles with A: Chuquicamata, B: Ilo, C: Caletones and D: Potrerillos.

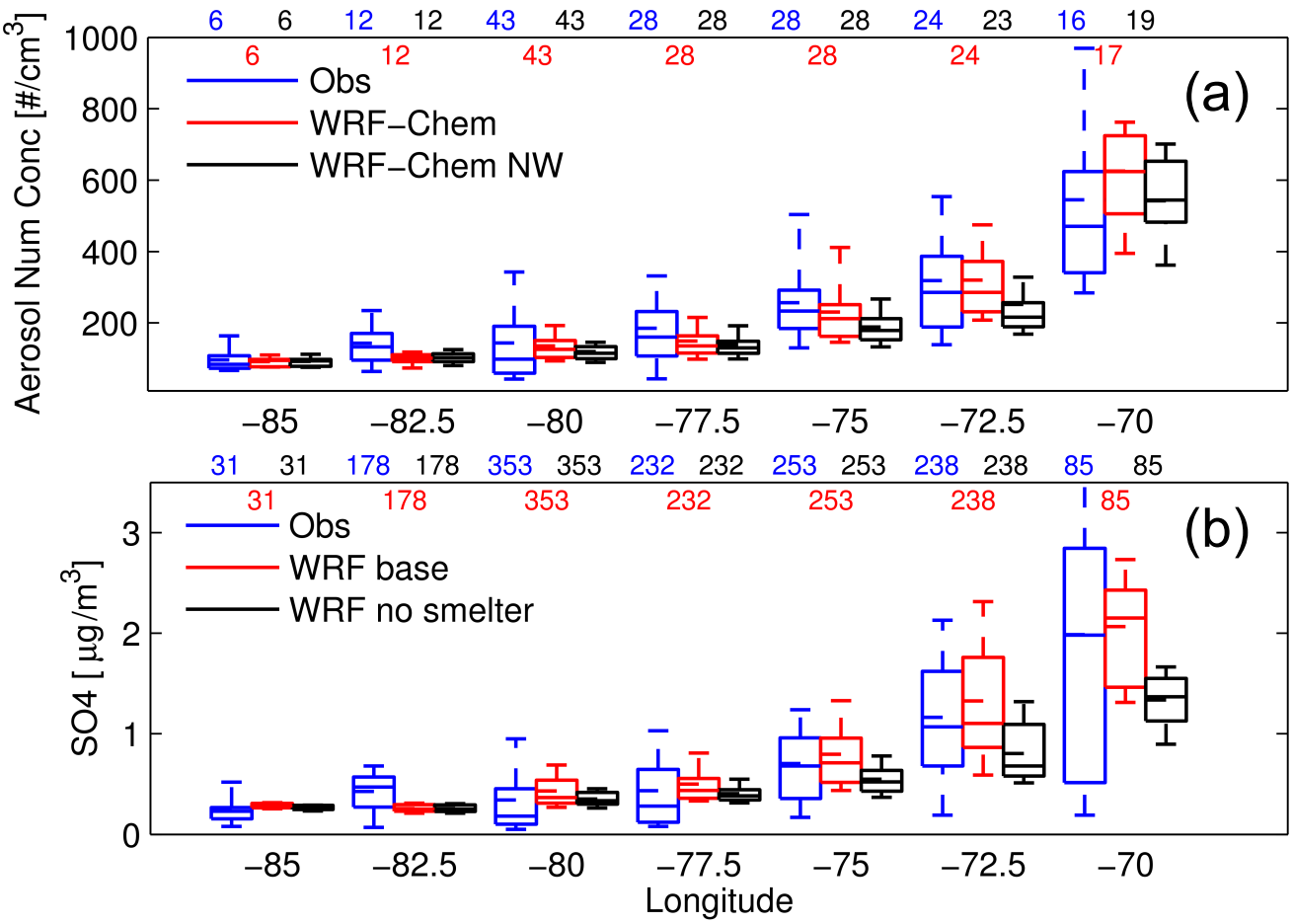

Fig. 7. a) Comparison of aerosol number concentration between 0.12 and 3.0 µm as observed from the C-130 (blue) vs. WRF-Chem model results with smelter emissions (red) and without smelter emissions (black) for the 15 Oct 2008 to 24 Oct 2008 time period. Data are gridded into 2.5 degree longitudinal zones between 22°S and 18°S. The number of profiles is indicated at the top of each longitude bin. b) Same but for measured (Allen et al., 2011) and modeled sulfate mass between 0.04 µm to 0.625 µm, with sampling time in minutes in each longitude bin indicated at the top. For each zone, center solid (dashed) lines indicate the median (mean), and boxes indicate upper and lower quartiles with upper and lower decile whiskers.

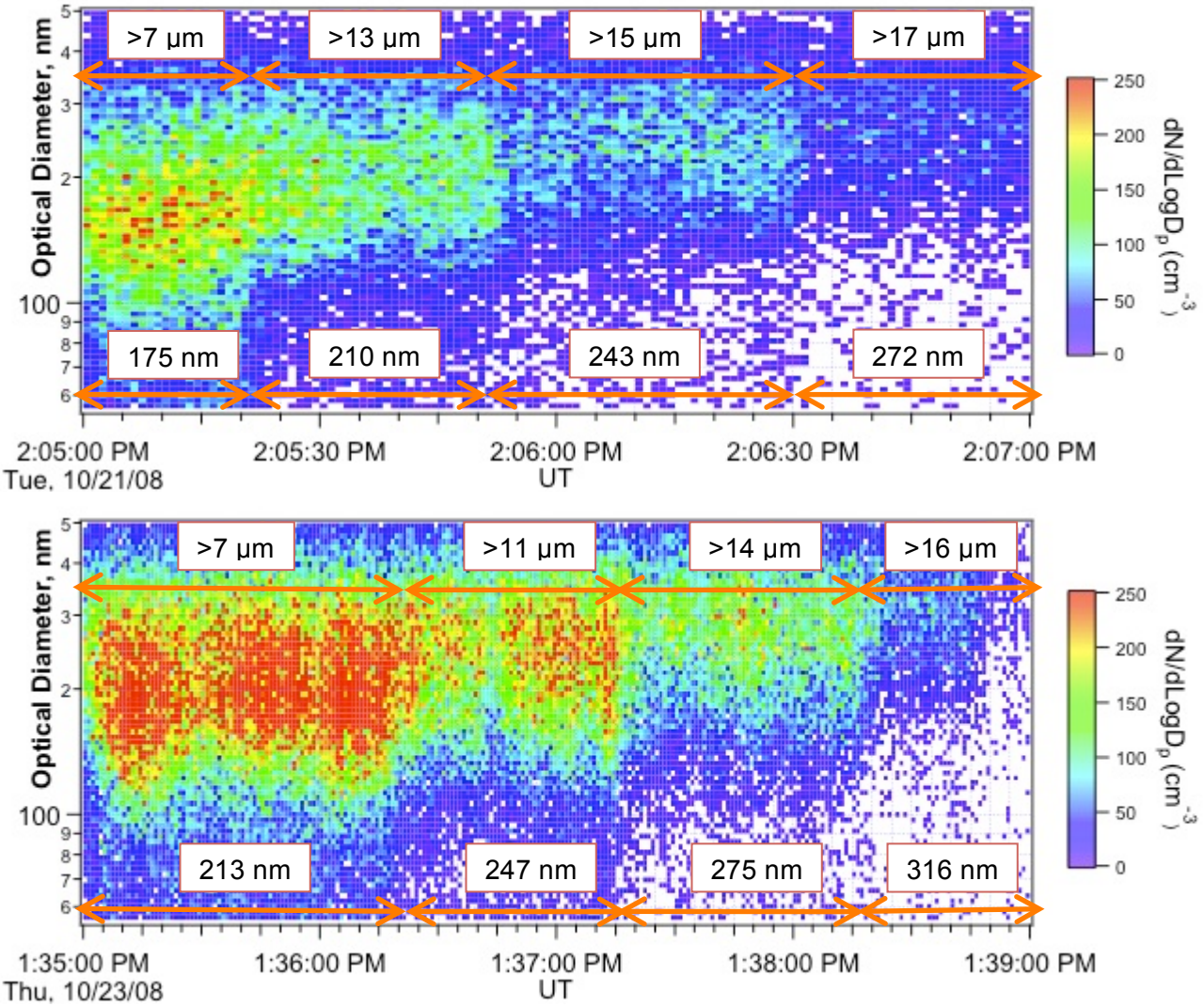

Fig. 8. Size distributions of droplet residual nuclei from droplets larger than different diameters as noted on the top of plots. Mean residual particle size is shown at bottom of plots. Top plot is from C-130 flight 3 (21 Oct 2008) and bottom is from flight 4 (21 Oct 2008).

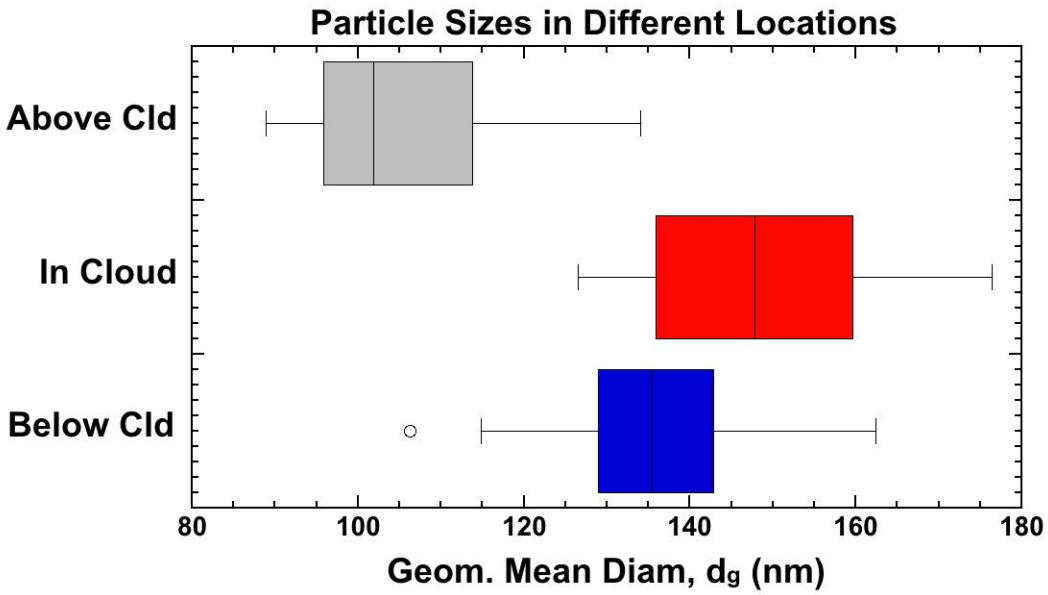

Fig. 9. Statistics of UHSAS geometric mean diameter for 20 pairs of below-cloud aerosol particles (blue) and CVI droplet residual nuclei (red) in VOCALS clouds with drizzle < 5 lit^{-1} and ratio of CVI total number concentration to droplet number concentration <1. Seventeen above-cloud samples are also shown in grey. The box limits represent the upper and lower quartiles, with the median as a horizontal line. The lines extending from the top and bottom of each box mark the maximum and minimum values within the data set that are within the upper quartile + (1.5 x the interquartile distance) or less than the lower quartile - (1.5 x the interquartile distance), respectively. Outliers are marked with circles.

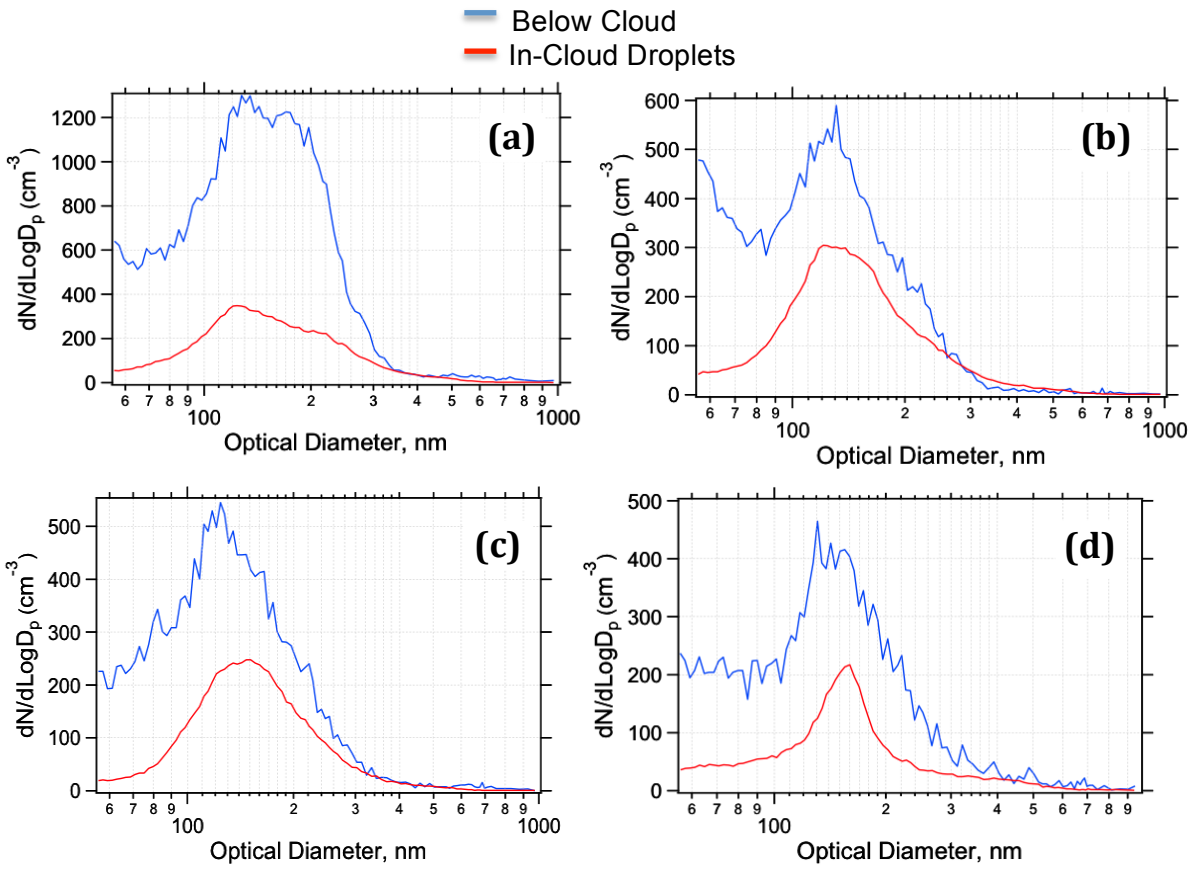

Fig 10. UHSAS particle size distributions for four sets of paired below-cloud (blue) and in-cloud droplets (red) CVI samples in clouds with drizzle < 5 lit^{-1} and ratio of CVI total number concentration to droplet number concentration between 0.72 and 0.94. C-130 flights and in-cloud UTC times are a) flight 2: 13:33:32-13:36:58, b) flight 3: 7:18:25-7:24:40, c) flight 3: 13:14:15-13:16:40, and d) flight 11: 16:42:42-16:47:22. In-cloud distributions are less noisy than below-cloud distributions due to the enhancement factor in the CVI inlet.

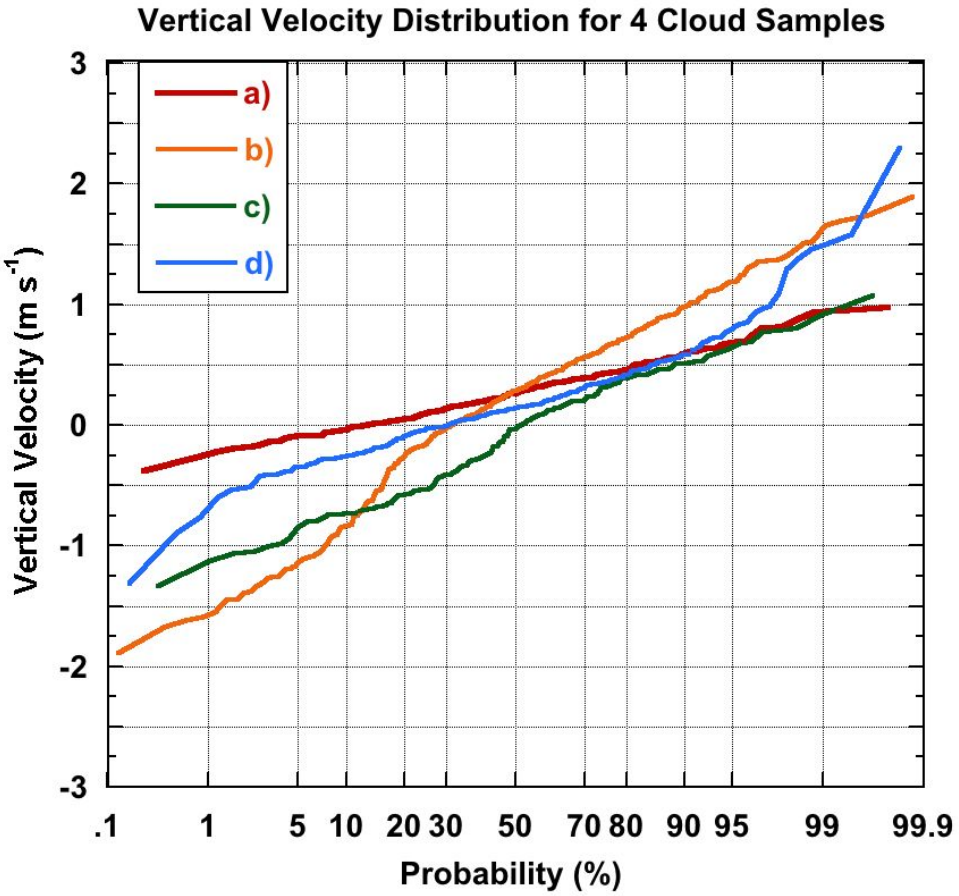

Fig. 11: Probability plot of vertical velocity (1 Hz) measured along the flight track for in-cloud samples a) through d) shown in Fig. 10.

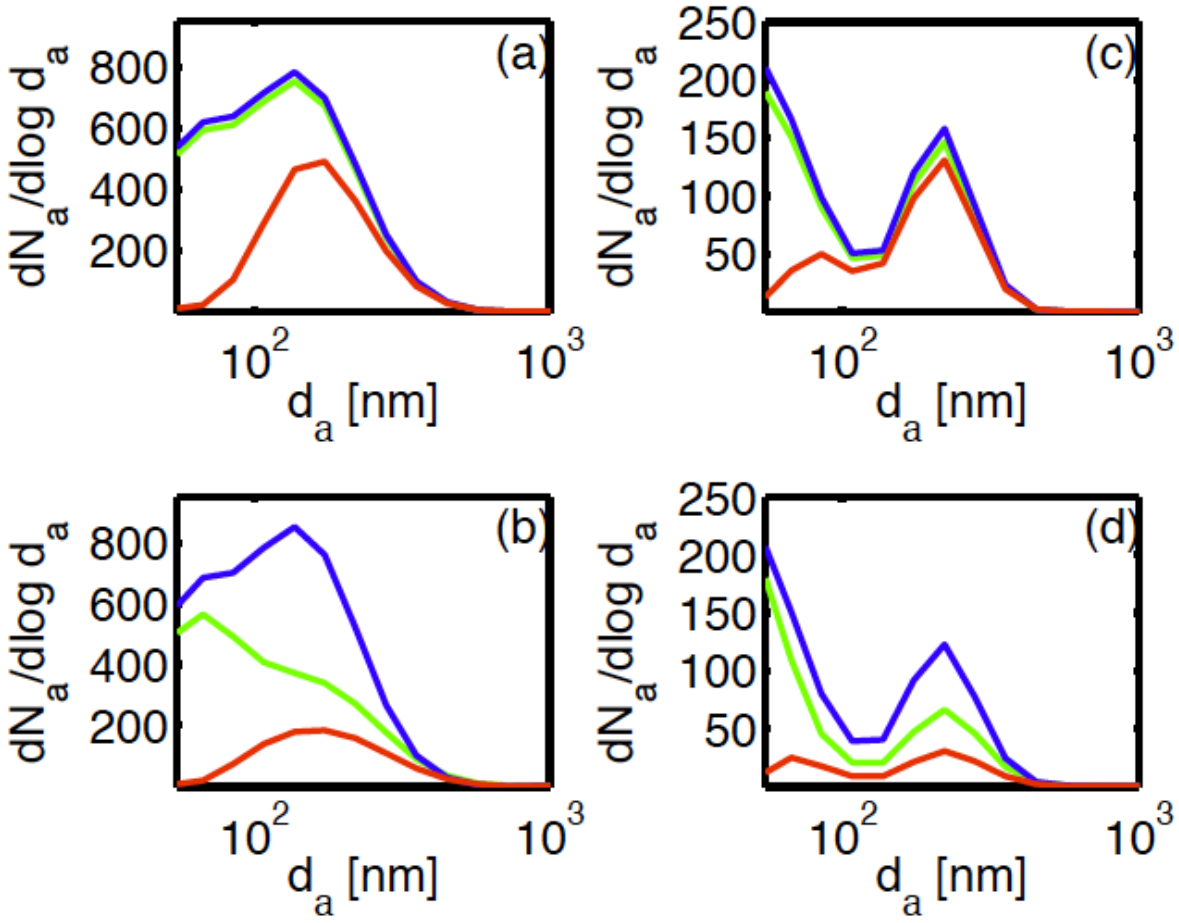

Fig. 12. Particles larger than 0.055 μm for HIGH (a,b) and LOW (c,d) Lagrangian cloud model cases after 2 hours (top) and 8 hours (bottom) of run time. Analogous to Fig. 10, the blue line shows the aerosol size distribution below the cloud, averaged between 100-350 m in height, while the red line represents the particles only present within droplets larger than 8 μm in size. The green line shows all particles within the cloud layer, including both interstitial and in-cloud particles. In-cloud was defined as points with $q_c > 10^{-6}$ g kg^{-1}.

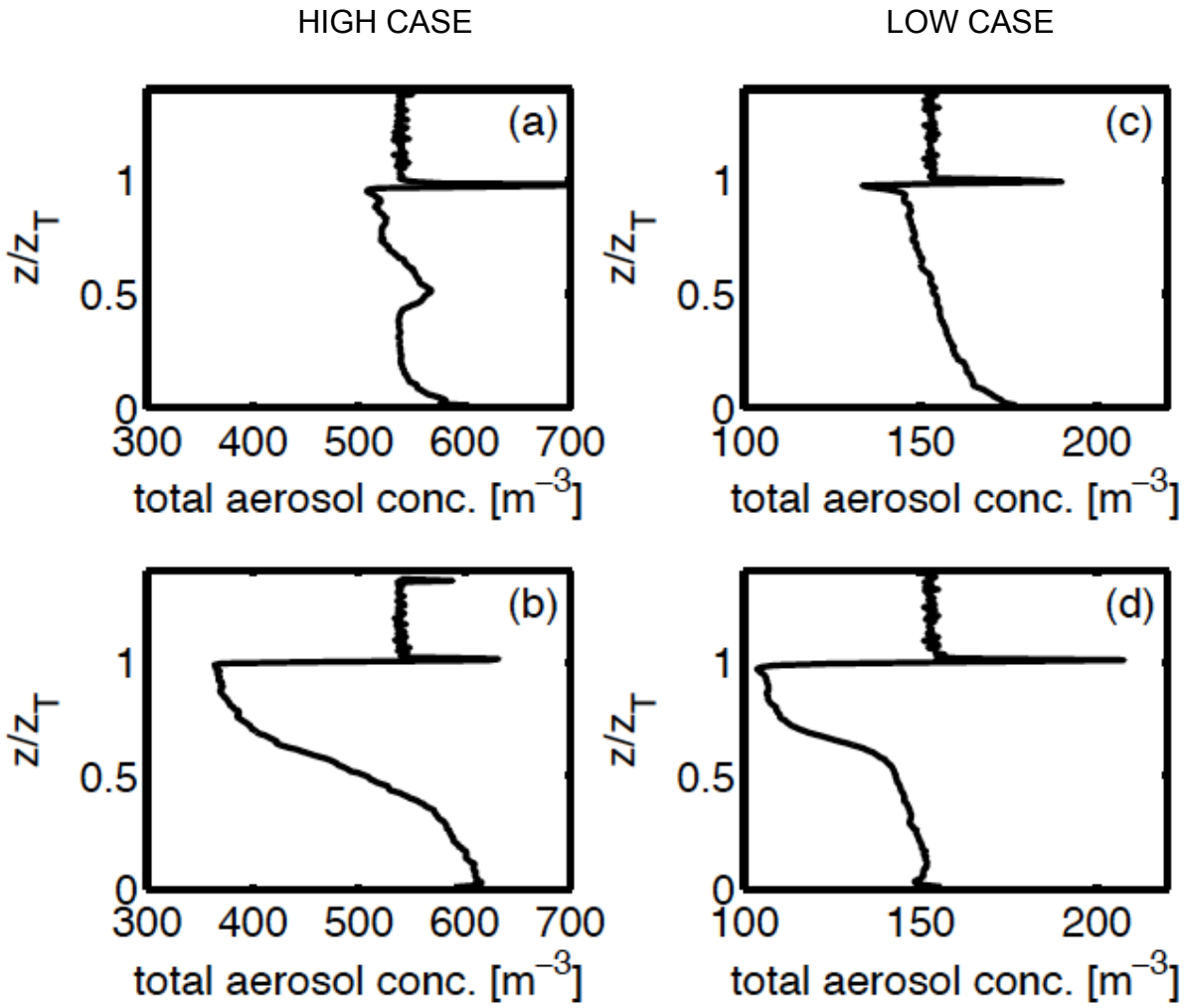

Fig. 13. Total aerosol concentration (ambient, interstitial and within droplets) predicted by the LCM after 2 hours (top, plots a and c) and 8 hours (bottom, plots b and d), as a function of height, scaled to the top of the cloud. HIGH aerosol case results are on the left and LOW aerosol case results are on the right.

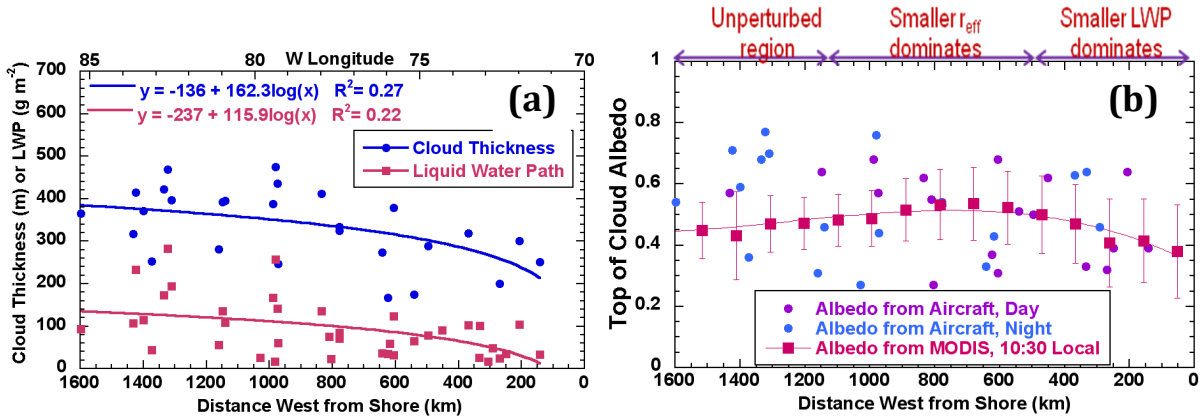

Fig 14. a. Cloud geometric thickness and liquid water path (LWP) as a function of distance west from shore along 20°S. Thickness is from the in-situ radar and lidar, while LWP uses both GVR and radar data. **b.** Top of cloud albedo vs. distance from shore calculated as described in the text (using 10:30 local values for solar zenith angle). Circles are values derived from onboard remote sensors during daytime (purple) and night-time (blue) C-130 flight segments, while red squares are derived from the MODIS 10:30 local overpass averaged over the entire VOCALS 31-day time period. Vertical bars represent one sigma variability in the MODIS data. Since in-cloud data only was used, cloud albedos here are higher than net albedos in partly cloudy regions.